A search for variability in exoplanet analogues and low-gravity brown dwarfs

Johanna M. Vos [1,2,3]* Beth A. Biller,[2,3] Mariangela Bonavita,[2,3] Simon Eriksson,[4] Michael C. Liu,[5] William M. J. Best,[5] Stanimir Metchev,[6] Jacqueline Radigan,[7] Katelyn N. Allers,[8] Markus Janson,[4] Esther Buenzli,[9] Trent J. Dupuy,[10] Mickaël Bonnefoy,[11] Elena Manjavacas,[12] Wolfgang Brandner,[13] Ian Crossfield,[14] Niall Deacon,[13,15] Thomas Henning,[13] Derek Homeier [,16] Taisiya Kopytova[17] and Joshua Schlieder[18]

Affiliations are listed at the end of the paper

ABSTRACT

We report the results of a *J*-band survey for photometric variability in a sample of young, low-gravity objects using the New Technology Telescope (NTT) and the United Kingdom Infrared Telescope (UKIRT). Surface gravity is a key parameter in the atmospheric properties of brown dwarfs and this is the first large survey that aims to test the gravity dependence of variability properties. We do a full analysis of the spectral signatures of youth and assess the group membership probability of each target using membership tools from the literature. This results in a 30 object sample of young low-gravity brown dwarfs. Since we are lacking in objects with spectral types later than L9, we focus our statistical analysis on the L0–L8.5 objects. We find that the variability occurrence rate of L0–L8.5 low-gravity brown dwarfs in this survey is 30^{+16}_{-8} per cent. We reanalyse the results of Radigan (2014) and find that the field dwarfs with spectral types L0–L8.5 have a variability occurrence rate of 11^{+13}_{-4} per cent. We determine a probability of 98 per cent that the samples are drawn from different distributions. This is the first quantitative indication that the low-gravity objects are more likely to be variable than the field dwarf population. Furthermore, we present follow-up J_S and K_S observations of the young, planetary-mass variable object PSO 318.5–22 over three consecutive nights. We find no evidence of phase shifts between the J_S and K_S bands and find higher J_S amplitudes. We use the J_S light curves to measure a rotational period of 8.45 ± 0.05 h for PSO 318.5–22.

Key words: brown dwarfs – stars: variables: general.

1 INTRODUCTION

Time-resolved photometric variability monitoring is a key probe of atmospheric inhomogeneities in brown dwarf atmospheres, as it is sensitive to the spatial distribution of condensates as a brown dwarf rotates. Photometric variability has been well studied in the more massive field L and T spectral type dwarfs, but the variability properties of the population of younger, low-gravity objects are less understood.

Radigan et al. (2014) reported the results of a large, ground-based search for *J*-band variability in L and T dwarfs, finding that 9 out of 57 (16 per cent) objects showed significant variability above photometric noise. Furthermore, the authors report enhanced variability frequency and amplitudes at the L/T transition, supporting

the hypothesis that cloud holes contribute to the abrupt decline in condensate opacity and *J*-band brightening observed at the L/T transition (however subsequent variability studies have shown that varying cloud layers, as opposed to holes, are responsible for observed variability; Apai et al. 2013; Buenzli et al. 2015). Wilson, Rajan & Patience (2014) presented a similar ground-based variability survey, the *Brown Dwarf Atmospheric Monitoring* (BAM) survey, which monitored 69 brown dwarfs spanning L0 to T8. Significant variability was reported in 14 of 69 objects (20 per cent), with no evidence for an enhancement in frequency or amplitude across the L/T transition. However, Radigan (2014) carried out a reanalysis of the 13 highly variable objects reported by Wilson et al. (2014) and found significant variability in only 4 from 13. Combining the revised BAM survey with the Radigan et al. (2014) survey, Radigan (2014) found that 24^{+11}_{-9} per cent of objects in the L9–T3.5 range exhibit *J*-band variability, in contrast to $2.9^{+4.1}_{-2.1}$ per cent of L0–

* E-mail: jvos@amnh.org

L8.5 brown dwarfs and $3.2^{+4.4}_{-2.3}$ per cent of T4–T9.5 brown dwarfs. Buenzli et al. (2014) presented a 22 target *HST* grism spectroscopy survey at wavelengths of 1.1–1.7 µm, attaining point-to-point precision of 0.1–0.2 per cent during ∼40 min observations. Low-level (∼1 per cent) variability trends were detected in six brown dwarfs (27 per cent), with no evidence for enhanced frequency across the L/T transition, suggesting that low-level heterogeneities are a frequent characteristic of brown dwarf atmospheres across the entire L–T spectral range. Metchev et al. (2015) reported results from a *Spitzer* program to search for photometric variability in a larger sample of 44 L3–T8 dwarfs at 3.6 and 4.5 µm, reaching 0.2–0.4 per cent precision. Metchev et al. (2015) reach a similar conclusion, finding that photometric variability is common among L and T dwarfs. The survey included eight low- or intermediate-gravity brown dwarfs to probe the effects of low surface gravity on the variability properties of brown dwarfs. A tentative correlation was found between low-gravity and high-amplitude variability, however a larger sample is necessary to confirm this potential relation (Metchev et al. 2015).

For the majority of directly imaged exoplanets, the contrast between host star and planet make it difficult to obtain sufficiently high S/N photometry to allow detailed studies of their variability, thus only a handful are amenable to variability studies. In fact, Apai et al. (2016) explored the rotational variability of the HR8799 planets, reaching a photometric precision of ∼10 per cent, thus insufficient to detect variability on levels of a few per cent. However, young brown dwarfs provide an excellent analogue to directly imaged exoplanets. Recently, a handful of young brown dwarfs with colours and magnitudes similar to directly imaged planets have been discovered (see compilation of young objects made by Faherty et al. 2016; Liu, Dupuy & Allers 2016). The atmospheres of these young brown dwarfs can provide insight into the atmospheres of directly imaged planets. Like their higher mass brown dwarf counterparts (Zapatero Osorio et al. 2006), young companion exoplanets and free-floating objects appear to be fast rotators with measured rotational periods of ∼7–11 h (Snellen et al. 2014; Biller et al. 2015; Allers et al. 2016; Zhou et al. 2016). This makes them excellent targets for photometric variability monitoring.

Variability has now been detected in a small sample of low-gravity objects. As part of this survey, variability was detected in the planetary-mass object PSO J318.5338–22.8603 (PSO 318.5–22; Biller et al. 2015). With a variability amplitude of 7–10 per cent, PSO 318.5–22 displays a very high variability amplitude compared to most objects in the field population. This was swiftly followed by a variability detection in the 3 M_{Jup} companion 2MASSW J1207334–393254 (2M1207b), which displayed ∼1.36 per cent variability in the *F*125*W* filter during a 9 h observation with *HST* (Zhou et al. 2016). The 19 M_{Jup} object WISEP J004701.06+680352.1 (W0047) was found to exhibit ∼8 per cent variability during a 9 h *HST* observation (Lew et al. 2016). Vos et al. (2018), reported results from a *Spitzer* program to monitor variability on the intermediate gravity late-L dwarfs W0047 and 2MASS J2244316+204343 (2M2244) and the planetary-mass T5.5 object SDSS 111010+011613 (SDSS1110). W0047 and 2M2244 were both found to be variable in the mid-IR, with fairly high amplitudes compared to the sample of higher mass field dwarfs that have been studied. There is also tentative evidence that the low-gravity T dwarfs exhibit higher variability amplitudes compared to field objects. Gagné et al. (2017) find that the highly variable object SIMP0136 is a likely member of the ∼200 Myr Carina-Near moving group. Gagné et al. (2018a) confirm the variable object 2M1324 as a member of the AB Doradus moving group and estimate a mass

of 11−12 M_{Jup}. Naud et al. (2017) obtained three 5−6 h epochs of variability monitoring observations of the young T-type companion GU Psc b in AB Doradus. The authors detect marginal variability in one epoch but do not detect significant variability in the other two epochs. The high amplitudes observed in this small sample of low-gravity variable objects adds to the growing evidence that there is a link between low-gravity and enhanced variability.

Here, we present the results of the first photometric monitoring survey of young, low-gravity L and T dwarfs, with the goal of investigating the gravity dependence of variability properties. Observations were carried out at the 3.5 m New Technology Telescope (NTT) and the 3.8 m United Kingdom Infrared Telescope (UKIRT).

2 SAMPLE SELECTION

From Autumn 2014 to Spring 2017 we observed a sample of 36 brown dwarfs that are candidate members of young moving groups in the literature and/or show signatures of youth in their spectra. We present our observing log in Table 1. Our survey targets are primarily sourced from the BANYAN catalogues (Gagné et al. 2014a, 2015a) and Best et al. (2015). We additionally include the wide companions HN Peg B and GU Psc b (Luhman et al. 2007; Naud et al. 2014). The full survey sample is shown in Table 3. We consider the following young moving groups in this paper: TW Hydra (TWA, 10 ± 3 Myr; Bell, Mamajek & Naylor 2015), β Pictoris (β Pic, 22 ± 6 Myr; Shkolnik et al. 2017), Columba (Col, 42^{+6}_{-4} Myr; Bell et al. 2015), Tucana-Horologium (THA, 45 ± 4 Myr; Bell et al. 2015), Carina (Car, 45^{+11}_{-7} Myr; Bell et al. 2015), Argus (Arg, 30−50 Myr; Torres et al. 2008), AB Doradus (AB Dor, 110−150 Myr; Luhman et al. 2007; Barenfeld et al. 2013), and Carina-Near (CarN, 200 ± 50 Myr; Zuckerman et al. 2006). Our targets show signs of low gravity in their spectra and/or are candidate members of nearby young moving groups. We reassess the spectral and kinematic evidence of low gravity/youth for each object in Section 8.

To obtain high signal-to-noise (S/N) measurements that could be robustly compared to previous surveys (Radigan et al. 2014; Wilson et al. 2014), targets were limited to objects with magnitudes brighter than $J_{2MASS} = 17.0$ mag (apart from one target, GU Psc b). We observed our targets at airmasses <1.5 to maximize the S/N.

The sample consists of spectral types L0 and later, as these are less likely to exhibit magnetic spot activity due to the increasingly neutral atmospheres present in objects with T_{eff} below ∼2100 K. Gelino et al. (2002) and Miles-Páez et al. (2017) find no correlation between magnetic activity (in the form of Hα emission) and photometric variability in a sample of L and T dwarfs. We attempt to cover the entire L–T spectral range uniformly, however few young T dwarfs sufficiently bright for ground-based IR photometric monitoring are known, preventing us from fully covering the T spectral type. Thus, our sample is predominantly comprised of L-type objects.

There is only one known binary in our sample, 2MASS J03572695–4417305 (Bouy et al. 2003). The binary separation (≈0.1 arcsec) is less than the seeing so the photometry in this study records the combined flux from both components. The variability of one component in an unresolved binary will be diluted by flux from the non-variable component, making it more difficult to detect the variability. Alternatively, if both components of the binary are variable (as is the case for the Luhman 16AB binary system; Biller et al. 2013; Buenzli et al. 2015), their differing variability amplitudes and rotational periods will be combined in the observed light curve, likely resulting in a complex and/or rapidly evolving light curve.

Table 1. Observing log.

Target	Telescope	Band	Date	Δt	FWHM
2M0001+15	UKIRT	J	2016-10-12	3.75	1.01
2M0045+16	NTT	J_S	2014-11-11	4.05	1.30
2M0045+16	NTT	J_S	2015-08-17	3.36	0.56
2M0045+16	UKIRT	J	2016-11-13	4.36	0.94
2M0103+19	NTT	J_S	2014-11-03	5.28	0.40
GU Psc b	NTT	J_S	2014-10-11	3.46	0.83
2M0117−34	NTT	J_S	2014-11-08	4.44	0.44
2M0117−34	NTT	J_S	2016-10-18	1.92	2.26
2M0234−64	NTT	J_S	2014-11-10	5.59	0.63
2M0303−73	NTT	J_S	2014-11-09	5.50	0.49
2M0310−27	NTT	J_S	2014-11-08	3.00	0.46
2M0323−46	NTT	J_S	2014-11-07	5.32	1.07
2M0326−21	NTT	J_S	2014-11-04	4.68	0.51
2M0342−68	NTT	J_S	2014-11-03	2.88	0.44
PSO 057+15	UKIRT	J	2016-12-23	3.59	1.26
2M0355+11	NTT	J_S	2014-10-07	4.73	0.83
2M0357−44	NTT	J_S	2014-10-10	4.13	1.10
2M0418−45	NTT	J_S	2017-03-14	2.11	0.68
2M0421−63	NTT	J_S	2014-10-08	5.50	1.01
PSO071.8−12	NTT	J_S	2017-10-18	3.31	1.71
PSO071.8−12	UKIRT	J	2017-12-08	4.29	1.16
2M0501−00	NTT	J_S	2014-11-11	4.03	1.06
2M0501−00	NTT	J_S	2015-08-16	2.01	2.39
2M0501−00	NTT	J_S	2016-10-19	4.99	1.49
2M0501−00	NTT	J_S	2017-03-12	1.85	0.43
2M0512−27	NTT	J_S	2017-03-13	3.00	0.40
2M0518−27	NTT	J_S	2014-11-05	3.98	1.52
2M0536−19	NTT	J_S	2014-10-11	2.88	0.90
SDSS1110+01	NTT	J_S	2017-03-12	5.40	0.37
2M1207−39	NTT	J_S	2017-03-13	4.49	0.34
2M1256−27	NTT	J_S	2017-03-14	2.54	0.40
2M1425−36	NTT	J_S	2015-08-17	2.52	0.42
2M1425−36	NTT	J_S	2017-03-14	4.10	0.39
2M1615+49	UKIRT	J	2016-07-10	4.33	1.14
W1741	NTT	J_S	2014-10-11	2.37	0.67
PSO 272.4−04	NTT	J_S	2017-03-12	2.28	0.34
2M2002−05	UKIRT	J	2016-07-09	4.37	1.22
2M2011−05	NTT	J_S	2015-08-15	3.43	0.48
SIMP J2154	NTT	J_S	2014-11-07	3.44	1.12
HN Peg B	NTT	J_S	2014-10-08	3.88	1.17
HN Peg B	NTT	J_S	2015-08-17	1.42	0.58
HN Peg B	UKIRT	J	2016-07-11	4.97	1.00
HN Peg B	UKIRT	J	2016-07-13	5.01	1.00
PSO J318−22	NTT	J_S	2014-10-09	5.13	0.48
PSO J318−22	NTT	J_S	2014-11-09	2.83	0.42
PSO J318−22	NTT	K_S	2014-11-10	3.10	0.52
PSO J318−22	NTT	J_S	2015-08-16	4.99	0.38
PSO J318−22	NTT	J_S	2016-08-09	9.12	1.26
PSO J318−22	NTT	K_S	2016-08-10	9.65	1.44
PSO J318−22	NTT	J_S	2016-08-11	10.46	1.37
PSO J318−22	NTT	K_S	2016-08-11	9.84	1.22
2M2244+20	UKIRT	J	2016-07-21	4.10	1.13
2M2322−61	NTT	J_S	2014-10-10	4.37	1.28

3 OBSERVATIONS AND DATA REDUCTION

3.1 NTT SofI

The observations took place between 2014 October and 2017 March with the SofI (Son of Isaac) instrument, mounted on the 3.6 m NTT at La Silla Observatory. Observations were carried out in large field imaging mode, which has a pixel scale of 0.288 arcsec and a 4.92 arcmin × 4.92 arcmin field of view. Targets were observed

using the J_S band (1.16–1.32 μm). The J_S filter was chosen as it avoids contamination from the water band at 1.4 μm. Two targets were observed each night, alternating between nods in an ABBA pattern, with three exposures at each position. At each nod we ensured the target was accurately placed on the same original pixel in order to preserve photometric precision. 2−5 h observations were obtained for each target. The flux of the target was kept below 10 000 ADU to prevent any non-linearity effects.

The data reduction steps are outlined in the SofI manual, and an IRAF pipeline was provided by ESO. We processed our images using both the standard IRAF routine as well as an IDL version. Here, we detail our data reduction process.

3.1.1 Inter-quadrant row crosstalk

The SofI detector suffers from inter-quadrant row crosstalk, where a bright target imaged in one quadrant can cause a faint glow in equivalent rows of the other quadrants. The intensity of the crosstalk feature scales with the total intensity along a given row by an empirically determined value of 1.4×10^{-5} and can be removed easily.

3.1.2 Flat-fielding

The shade pattern on the array is a function of the incident flux, so the method of creating flat-fields by subtracting lamp-off from lamp-on dome flats leaves a residual shade pattern across the centre of the array. For this reason 'special' dome flats are taken using standard frames along with frames in which the array is partially obscured to estimate the illumination dependent shade pattern of the array. The shade pattern can be removed as described by the ESO documentation.

3.1.3 Illumination correction

Illumination correction removes the difference between the illumination pattern of the dome flat screen and the sky. This correction is determined from a grid of 16 observations of a standard star across the field of view. The illumination correction is created by fitting a 2D surface to the fluxes of the star after flat-fielding.

3.1.4 Sky subtraction

The sky subtraction of images obtained with SofI serves to remove the dark current as well as the illumination-dependent shade pattern. Sky frames are created by median combining normalized frames of different nods which are closest in time. These are then re-scaled to the science frame before being subtracted from the science frame.

3.1.5 Aperture photometry

The positions of the target star as well as a set of reference stars in the field of view were found in each frame using IDL FIND.PRO followed by GCNTRD.PRO to measure the centroids. Aperture photometry was performed on the target as well as the set of reference stars. Fixed apertures of sizes similar to the median FWHM of all stars on the chip were used. The final aperture was chosen to minimize the photometric noise.

The standard deviation provides a good estimate of noise for a non-variable light curve. However, the standard deviation of a variable light curve measures both noise and intrinsic variations, and hence overestimates the noise. We estimate the typical photometric

error for each light curve, σ_{pt}, using a method described by Radi-gan et al. (2014). This is the standard deviation of the light curve subtracted from a shifted version of itself, $f_{i+1} - f_i$, divided by $\sqrt{2}$. This quantity is sensitive to high-frequency noise in the data and is insensitive to the low-frequency trends we expect from variable brown dwarfs. Thus, it provides a more accurate estimate of the photometric noise for variable light curves.

3.2 UKIRT WFCAM

Observations of eight targets were taken with the infrared Wide-Field Camera (WFCAM; Casali et al. 2007). WFCAM is a wide-field imager on the 3.8 m UKIRT on Mauna Kea, with a pixel scale of 0.4 arcsec. The observations were carried out in the *J* band. Each target was observed using an ABBA nod pattern, as before. Frames were reduced using the WFCAM reduction pipeline (Irwin et al. 2008; Hodgkin et al. 2009) by the Cambridge Astronomy Survey Unit. The pipeline reduction steps include linearity correction, dark correction, flat-fielding, gain-correction, decurtaining, defringing, sky subtraction, and crosstalk removal (Irwin et al. 2004). We per-formed aperture photometry on the target and reference stars in the field of similar brightness, using a range of aperture sizes similar to the median FWHM of all stars in the field.

3.3 Light-curve analysis

The raw light curves obtained from aperture photometry display fluctuations in brightness due to changing atmospheric transparency, airmass, and residual instrumental effects. To a very good approxi-mation these changes are common to all stars in the field of view and can be removed via division of a calibration curve calculated from a set of iteratively chosen, well-behaved reference stars (Radigan et al. 2012). First, reference stars with peak flux values below 10 or greater than 10 000 ADU were discarded. Different nods were nor-malized via division by their median flux before being combined to give a relative flux light curve. For each star a calibration curve was created by median combining all other reference stars (excluding that of the target and star in question). The standard deviation and linear slope for each light curve was calculated and stars with a stan-dard deviation or slope ∼1.5–3 times greater than that of the target were discarded. This process was iterated a number of times, until a set of well-behaved reference stars was chosen. Final detrended light curves were obtained by dividing the raw curve for each star by its calibration curve. Light curves shown in this paper have been binned by a factor of 1–3.

3.4 Independent reduction of NTT/SofI data

We additionally present the results of an independent data reduction process outlined in the MSc thesis of Simon Eriksson and supervisor Markus Janson (Eriksson 2016). Twenty of the 21 targets observed with the NTT in 2014 were independently reduced and analysed. A further 10 observations from 2015 to 2017, mainly follow-ups, were investigated in late 2017 in the same way. Overall, 24 out of 30 NTT targets underwent reduction. The reduction steps previously outlined in Section 3.1.5 were performed, with the addition of a dark subtraction. The SofI pipeline provided by ESO was used for dark, flat-field and crosstalk corrections and sky subtraction. The process resulted in combined images of two different nods closest in time, and subsequent photometry was obtained using PHOT in IRAF. Errors were estimated from PHOT output together with a polynomial fitting to the light curves.
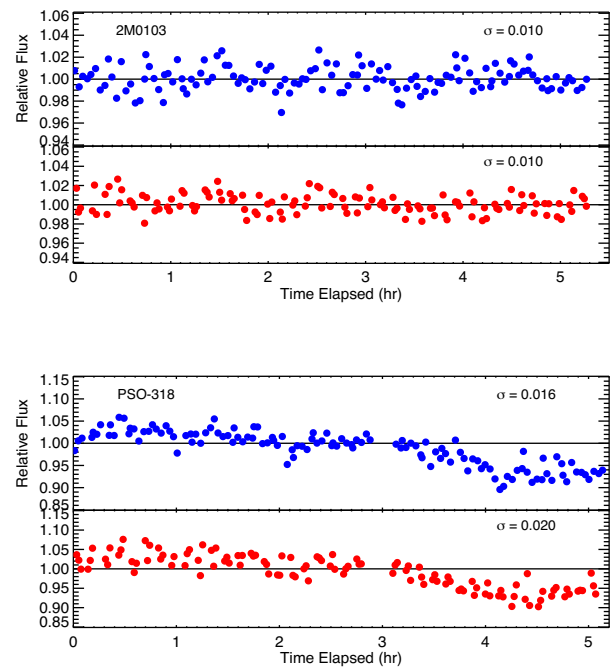

Figure 1. Light curves of 2M0103 and PSO–318 reduced and analysed using two methods. The blue points show the light curve obtained from the method described in Section 3.1 and the red points show the light curve obtained from the independent reduction described in Section 3.4. Both light curves are binned by a factor of 2. The same light-curve shape and a similar photometric error σ is recovered for each observation.

In Fig. 1, we compare the light curves of two objects in our survey that were analysed using both reductions – the non-variable object 2M0103 (although Metchev et al. (2015) report low-amplitude mid-IR variability in this object) and the variable object PSO 318.5–22. The blue points show the light curve obtained from the method described in Section 3.1 and the red points show the light curve obtained from the independent reduction described above. Both methods produce the same light-curve shape and a similar photo-metric error σ. Since the results were consistent between reductions, for the rest of the paper we present light curves obtained using the method described in Sections 3.1 and 3.3.

3.5 Identification of variables

Variable targets were identified using a method similar to the peri-odogram analysis outlined in Vos et al. (2018). The periodograms of each target and its respective reference stars are plotted to identify periodic variability. For each observation, the 1 per cent false-alarm probability (FAP) is calculated from 1000 simulated light curves. These light curves are produced by randomly permuting the in-dices of the reference star light curves (Radigan et al. 2014). The 1 per cent FAP value is the periodogram power above which only 1 per cent of the simulated light curves fall. This method assumes Gaussian-distributed noise in the reference stars, however to assess the significance of residual correlated noise in the reference star light curves we measure the β factor of every light curve, which is the peak periodogram power of each reference star divided by the 1 per cent FAP power (Radigan et al. 2014). Fig. 2 shows the β factor of reference stars and targets for NTT (top) and UKIRT (bot-tom) observations. We display these separately as each instrument has unique systematics. For reference stars exhibiting Gaussian-
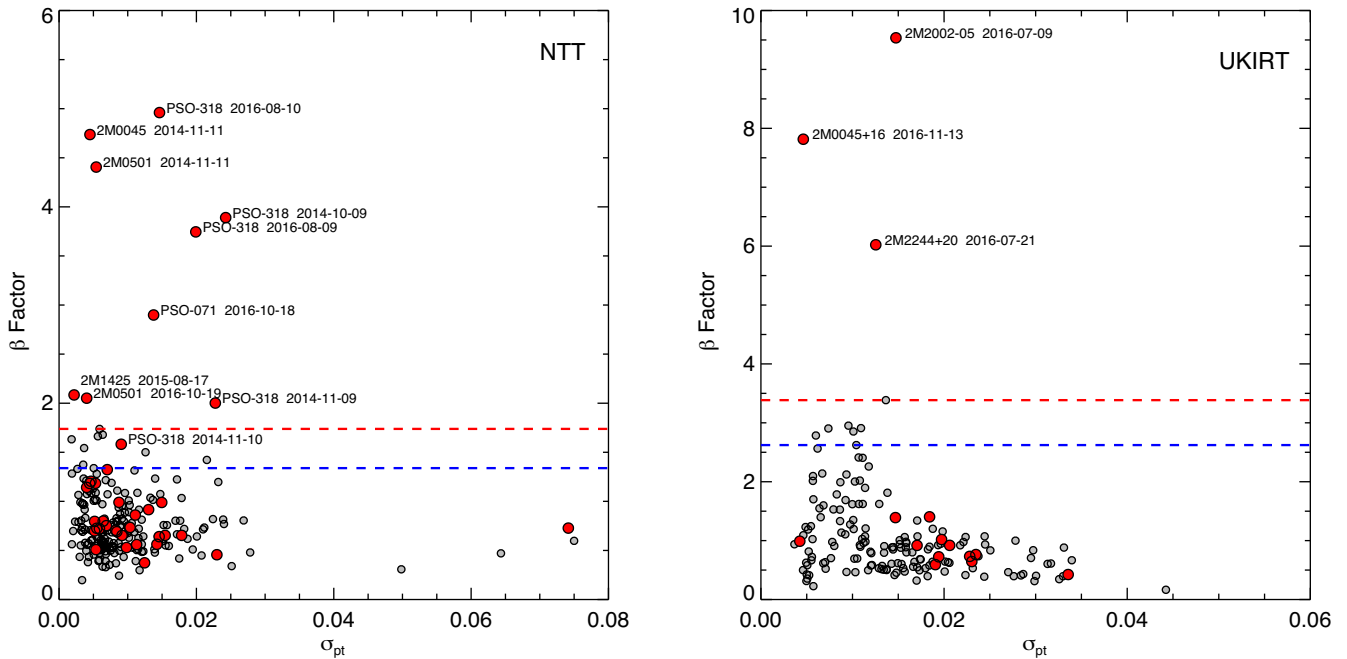
Figure 2. β factor plotted against the photometric error, σ_{pt}, for reference stars (grey circles) and targets (red circles) for the NTT (left) and UKIRT (right) samples. The β factor is defined as the periodogram peak power of each reference star divided by 99 per cent significance as calculated from our simulations. The updated, empirical 99 per cent and 95 per cent significance thresholds are shown by the red and blue dashed lines, respectively.

distributed noise, we would expect that 1 per cent of reference star peak powers would fall above $\beta = 1$, however for both samples more than 1 per cent of reference star peak powers fall above $\beta = 1$, and this is likely due to residual correlated noise in the light curves. To account for this excess noise, we find the empirical 1 per cent FAP by finding the β factor above which 1 per cent of reference star peak powers fall. Blue and red dashed lines indicate the new, empirical 95 per cent and 99 per cent significance thresholds. This increases the 99 per cent significance thresholds by a factor of 1.7 and 3.4 for the NTT and UKIRT samples, respectively.

We additionally explore an alternative method for identifying significantly variable objects, following a method described in Heinze, Metchev & Kellogg (2015) in a survey for optical variability in T-type brown dwarfs. In this study, the authors find a weak dependence of their variability metric on the RMS of each target. We can also see this in Fig. 2, where reference stars with a higher photometric error tend to have lower β factors. We thus investigate the dependence of the periodogram power on σ_{pt} (defined in Section 3.1.5). We can expect some dependence because if two light curves vary with the same amplitude but different noise levels, the light curve with lower photometric error produces a periodogram with a higher power. Thus, we take this into account in our significance threshold criteria. We show the peak periodogram power of targets and reference stars in Fig. 3. We calculate a σ-dependent 95 per cent threshold using a sliding box as described in Heinze et al. (2015). The box width was chosen such that >50 reference star points were available to calculate the 95 per cent threshold up to 0.02 σ_{pt} and 0.03 σ_{pt} for the NTT and UKIRT data, respectively. We find that a box width of 0.02 σ_{pt} is suitable for both. We show the noise-dependent 95 per cent significance threshold by the purple line in Fig. 3. Both methods identify the same variable objects with the exception of PSO 071.8–12 and GU Psc b. PSO 071.8–12 is identified as variable in the β factor method but is identified as non-variable in the noise-dependent periodogram power method. We count this

object as variable since the light curve shows high-amplitude modulation. It is likely that the periodogram power is low because PSO 071.8–12 has a rotational period that is significantly longer than the observation duration. GU Psc b is identified as variable in the noise-dependent method shown in Fig. 3. With a magnitude of $J = 18.12$, GU Psc b is at least an order of magnitude fainter than the other targets in our survey and as such, has a much higher photometric error than the other survey targets. Additionally, we have very few reference stars at $\sigma_{pt} > 0.03$, so calculating a 95 per cent threshold at values greater than this is not valid. For these reasons we do not count GU Psc b as a detection. Thus, we have detected variability in 13 epochs of observations, finding 7 variable objects in the survey. We show the light curves of each variable object and three reference stars in Fig. 4.

4 PERIODOGRAM ANALYSIS AND ROTATIONAL PERIODS

Manjavacas et al. (2018) find that the Lomb-Scargle periodogram method is sensitive to gaps in their *HST* light curve of a brown dwarf companion. The authors find that the publicly available Bayesian Generalised Lomb–Scargle method (BGLS; Mortier et al. 2015) is insensitive to these gaps, and produces a strong peak at the true rotational period of the brown dwarf. As some of our variable light curves have gaps in the data due to bad weather and/or instrumental difficulties at the telescope, we use the BGLS periodogram method to confirm that the detected trends are real, and not due to gaps in the data. The BGLS method produces periodograms with strong peaks at periods that are consistent with those of the Lomb–Scargle method for each variability detection. Thus, we can conclude that the periodicity observed in the periodograms is not due to gaps in the light curve.

While periodogram analysis can be used to provide an estimate of the rotational periods of brown dwarfs (e.g. Croll et al. 2016;
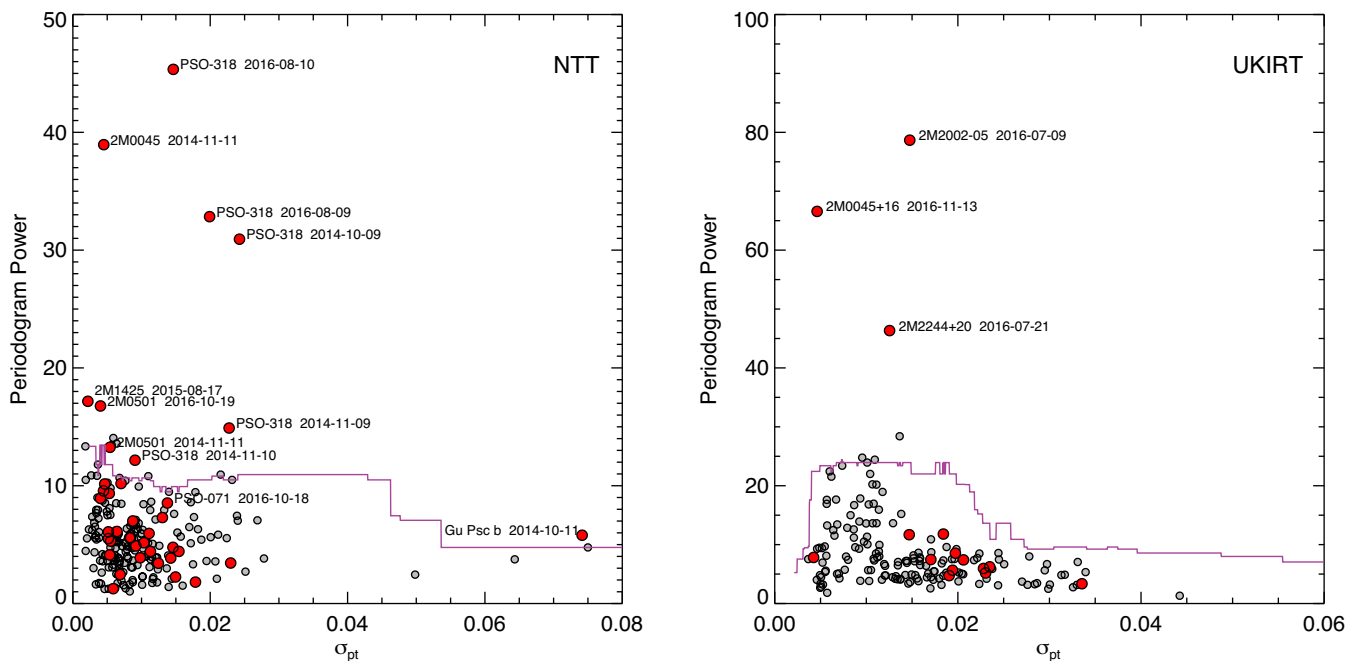
Figure 3. Maximum periodogram power plotted against the photometric error, σ_{pt}, for reference stars (grey circles) and targets (red circles) for the NTT (left) and UKIRT (right) samples. The σ_{pt}-dependent 95 per cent significance is shown by the purple line.

Manjavacas et al. 2018), we caution that the observation duration of our light curves are too short to robustly measure a period for most cases. Many of the variable light curves shown in Fig. 4 do not exhibit a local maximum or minimum and thus we can only place lower limits on their rotational periods. For light curves that do appear to exhibit local maxima or minima, the rotational periods cannot be confidently measured because double-peaked and evolving light curves have been observed in many variable brown dwarfs to date (e.g. Apai et al. 2017; Vos et al. 2018). Longer duration follow-up observations are necessary to robustly measure the rotational periods of the variable objects detected in this survey.

5 SENSITIVITY TO VARIABILITY SIGNALS

We construct a sensitivity plot for each observation to determine our sensitivity to variability signals of given amplitudes and periods. We inject simulated sinusoidal curves into random permutations of each target light curve. For targets found to be variable in the survey we divide the light curve by a polynomial fit to the light curve before injecting the simulated sinusoidal signals. The 1000 simulated sine curves have peak-to-peak amplitudes of 0.5–10 per cent and periods of 1.5−20 h, with randomly assigned phase shifts. Each simulated light curve is put through our periodogram analysis, which allows us to produce a sensitivity plot, showing thepercentage of recovered signals as a function of amplitude and period. Sensitivity plots for all light curves are shown in the bottom panel of Fig. 5 for variable objects and Fig. A3 (available online) for non-variables in the survey.

6 SIGNIFICANT DETECTIONS OF VARIABILITY

We detect significant variability in seven objects in the survey. Variable objects and their estimated variability amplitudes are presented in Table 2. We present the light curves of these variable objects along

with their reference stars in Fig. 4. We show their periodograms and sensitivity plots in Fig. 5. We discuss the first epoch variability detection of each object below.

2MASS J00452143+1634446 – Gagné et al. (2014a) classify the L2 object 2M0045+16 as a very low gravity brown dwarf, with H α emission and unusually red colours. It has been identified as a bona fide member of the Argus association (30−50 Myr), giving it an estimated mass of 14.7 ± 0.3 M_{Jup} (Gagné et al. 2015a), however recent work by Bell et al. (2015) has called into question the validity of the Argus association. We observed 2M0045+16 on 2014 November 11 using NTT SofI. We detect highly significant variability in this object at this epoch. The light curve of 2M0045+16 and the reference stars used for detrending are shown in Fig. 4 and the periodogram and sensitivity plots are shown in Fig. 5. A lack of stars in the field resulted in only three references stars suitable for detrending the light curve. We fit a sinusoid to the light curve using a Levenberg–Marquardt least-squares algorithm to estimate the amplitude of the modulation in the first epoch. This gives an amplitude of 1.0 ± 0.1 per cent and a period 4.3 ± 0.3 h. While it appears that we have covered a full rotational period, additional longer duration observations are necessary to rule out the possibility of a double-peaked light curve with a longer rotational period (e.g. Vos et al. 2018). We discuss follow-up observations of 2M0045+16 in Section 10.

PSO J071.8769−12.2713 – PSO 071.8−12 was identified as a high-probability candidate member of β Pictoris by Best et al. (2015). Assuming membership of the β Pictoris moving group, it has an estimated mass of 6.1 ± 0.7 M_{Jup} (Best et al. 2015), making it the lowest mass object to date to exhibit photometric variability. The light curve shown in Fig. 4 displays high-amplitude (4.5 ± 0.6 per cent) variability. The periodogram shown in Fig. 5 shows a highly significant (> 99 per cent) peak. Since we did not cover a full rotational period we can only estimate a period >3 h. We discuss subsequent follow-up observations of this object in Section 10.
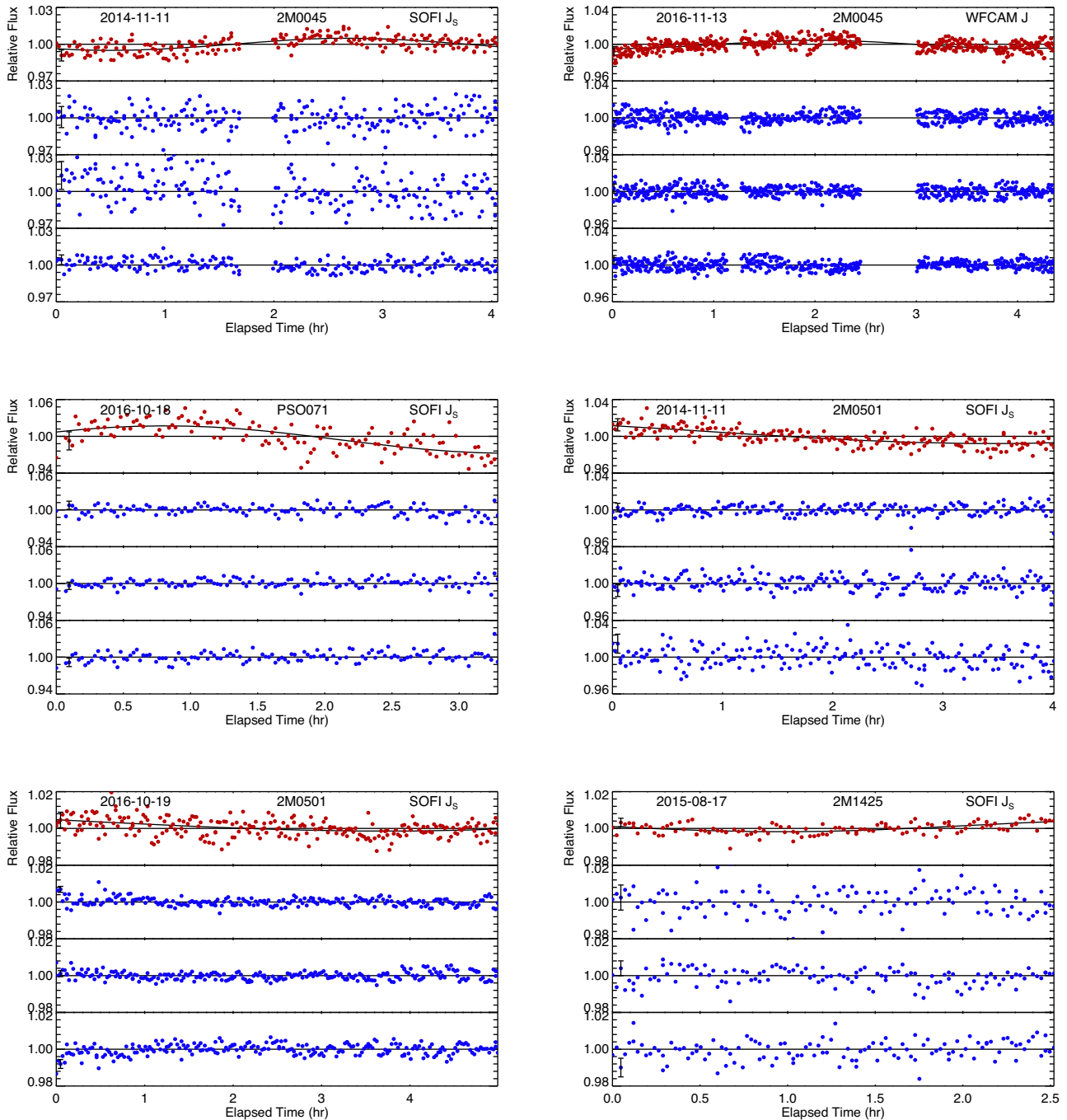
Figure 4. Light curves of variable targets (red) compared to a sample of reference stars in the field (blue). The black line shows the least-squares best-fitting sinusoidal model to the light curve.

2MASS J05012406−0010452 – Gagné et al. (2015a) categorize 2M0501–00 as L3γ, and an ambiguous candidate member of Columba or Carina (both moving groups are coeval at 20−40 Myr). If 2M0501–00 is indeed a member of Columba or Carina it has an estimated mass of $10.2^{+0.8}_{-1.0}$ M$_{Jup}$. We detect significant variability in 2M0501–00 on 2014 November 11 with NTT SofI (shown in Fig. 4). The periodogram shown in Fig. 5 shows a highly significant peak at periods >4 h. A sinusoidal fit to the light curve gives a peak-to-peak amplitude of 2.0 ± 0.1 per cent and a period of >4 h. Since we did not cover a full period of rotation in either epoch, our amplitude measurement is a lower limit and our period estimate

is very uncertain. We obtained additional follow-up monitoring of 2M0501–00 and discuss these observations in Section 10.

2MASS J14252798−36502295.23 – 2M1425–36 is classified as a bona fide member of AB Doradus (Gagné et al. 2015a). Radigan et al. (2014) previously reported 2M1425–36 as a marginal variable, displaying low-level variability over a ∼2.5 h observation. We detect low-amplitude variability in the L4 object 2M1425–36 on 2015 August 17. Fig. 5 shows a highly significant periodogram peak that favours a period of ∼3 h. Using our least-squares algorithm we estimate a variability amplitude of 0.7 ± 0.3 per cent for this epoch. We place a lower limit of 2.5 h on the rotational period since we did
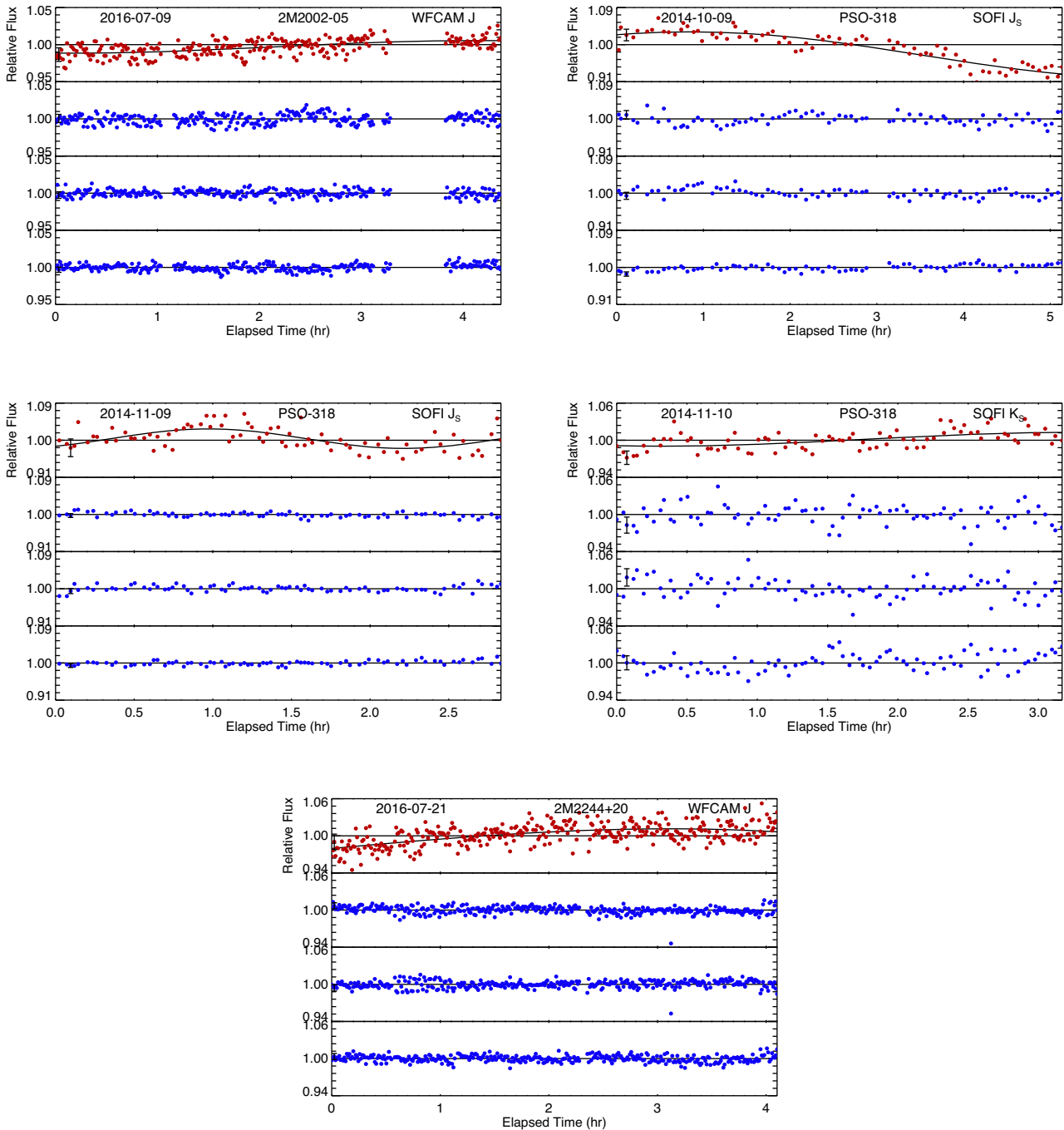
Figure 4. *Continued.*

not cover a full period. We observed 2M1425–36 a second time in 2017 and discuss this observation in Section 10.

2MASS J20025073−0521524 – 2M2002–05 is classified as an L5–L7 γ object by Gagné et al. (2015a), but has not been identified as a candidate of a young moving group (Faherty et al. 2016). Our UKIRT/WFCAM observation of this object taken on 2016 July 9 shows significant variability. Fitting a sinusoid to the light curve we estimate an amplitude of 1.7 ± 0.2 per cent and a period of 8 ± 2 h, however these are very uncertain as we did not cover a full rotational period in this epoch.

PSO J318.5338−22.8603 – Allers et al. (2016) confirm the L7 PSO 318.5–22 as a member of the 23 ± 3 Myr (Mamajek & Bell

2014) β Pictoris moving group. This implies a mass estimate of 8.3 ± 0.5 M_{Jup}, placing PSO 318.5–22 clearly in the planetary-mass regime. The light curves of PSO 318.5–22 from 2014 are presented in Biller et al. (2015) and are also included in this paper in Fig. 4. As discussed in Biller et al. (2015), we detect significant, high-amplitude variability in PSO 318.5–22 on 2014 October 9. The periodogram in Fig. 5 shows a highly significant peak at periods >4.5 h. A sinusoidal fit to the light curve gives a peak-to-peak amplitude of 10 ± 1.3 per cent and a period of 10 ± 2 h. We obtained two additional epochs of follow-up monitoring for PSO 318.5–22 as part of the variability survey and discuss these observations in Section 10.
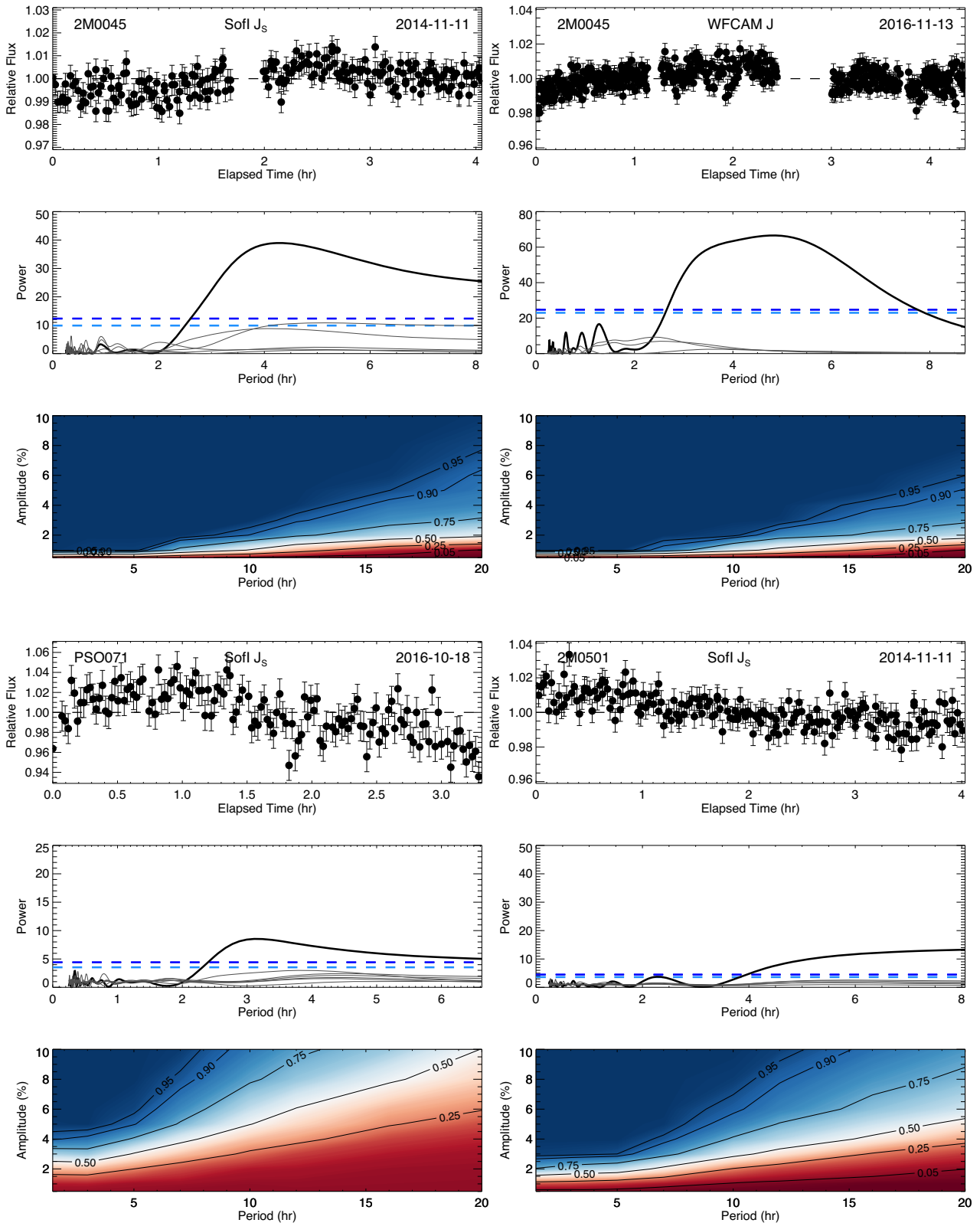
Figure 5. Light curves, periodograms, and sensitivity plots for variable objects. *Top panel:* Relative photometry of target. *Middle panel:* Periodogram of target light curve (black) and periodograms of reference stars (grey). Blue dashed lines show the 95 per cent and 99 per cent significance thresholds. *Bottom panel:* Sensitivity plot showing the percentage of recovered signals for injected sinusoidal signals of various variability amplitude and periods.
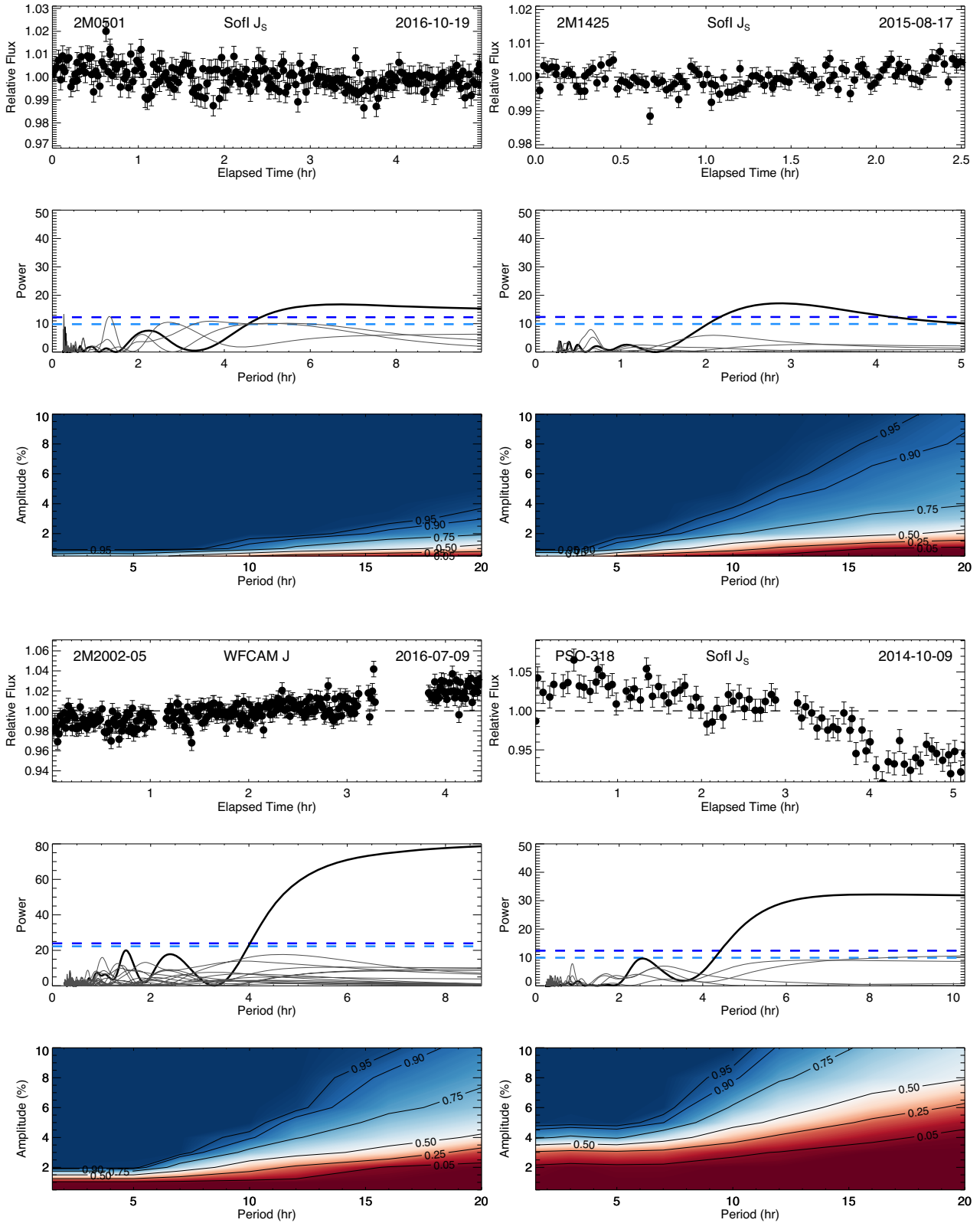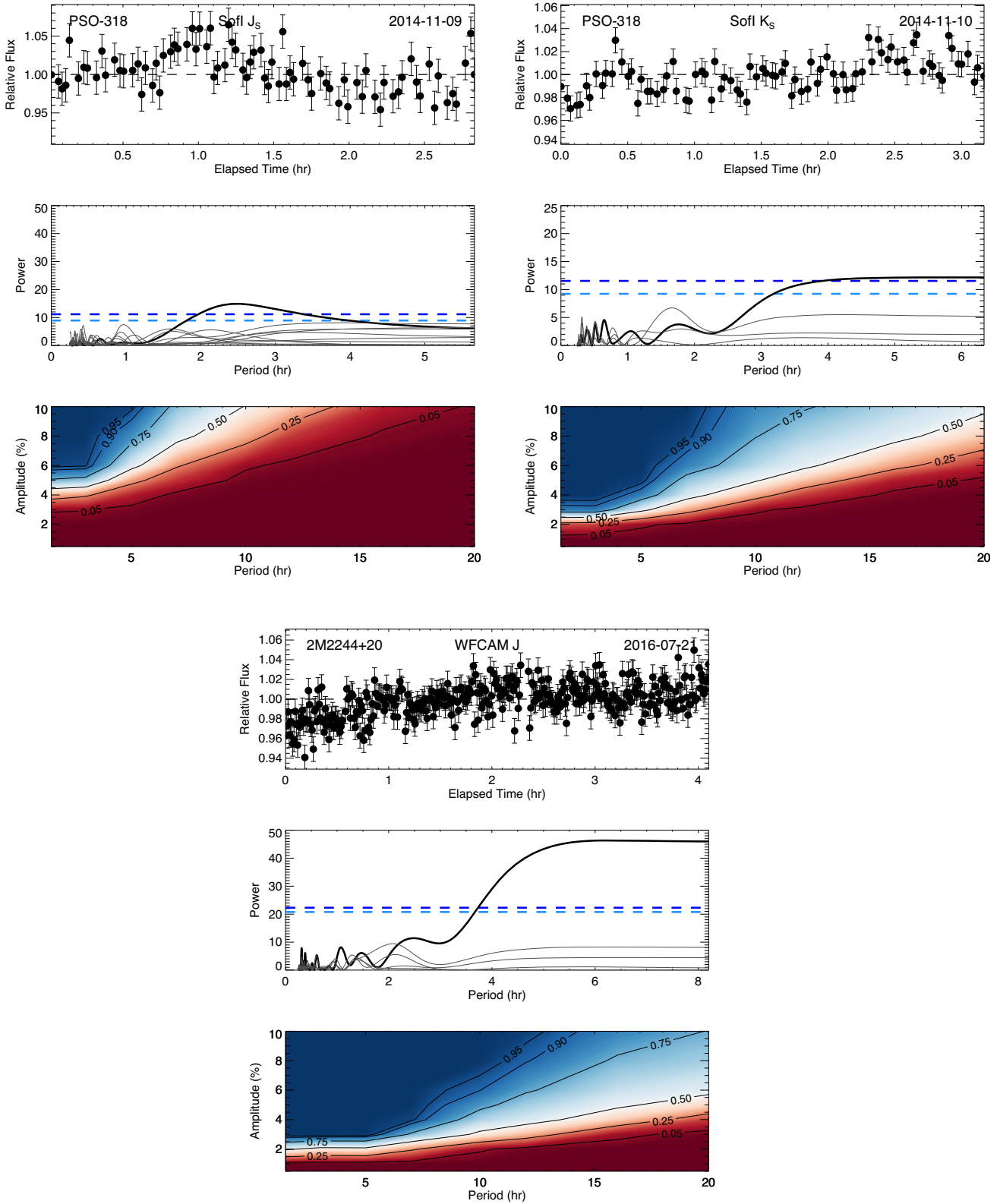
Figure 5. *Continued.*

Figure 5. *Continued.*

Table 2. Measured first epoch variability amplitudes for variability detections.

Target	Spt	Amp (per cent)
2M0045+16	L2	1.0 ± 0.1
PSO 071.8−12	T2	4.5 ± 0.6
2M0501−00	L3	2 ± 1
2M1425−36	L4	0.7 ± 0.3
2M2002−05	L5.5	1.7 ± 0.2
PSO 318.5−22	L7	10 ± 1.3
2M2244+20	L6–L8	5.5 ± 0.6

2MASS J2244316+204343 – 2M2244+20 is a confirmed member of AB Doradus, with an estimated mass of ∼19 M$_{Jup}$ (Vos et al. 2018). Morales-Calderon et al. (2006) and Vos et al. (2018) detect variability in the *Spitzer* 4.5 and 3.6 μm bands, respectively. The *J*-band light curve obtained in this survey was initially presented in Vos et al. (2018), where we measured a period of 11 ± 2 h for this object using *Spitzer* data. The UKIRT/WFCAM light curve obtained on 2016 July 21 shows significant variability. The periodogram shown in Fig. 5 shows a significant peak for periods >4 h. We set the period to 11 ± 2 h (as measured in Vos et al. 2018) in our least-squares sinusoidal fit and find an amplitude of 5.5 ± 0.6 per cent for this epoch.

7 NON-DETECTIONS

We present light curves and reference star light curves of non-variables in Fig. A1 (available online). Periodograms and sensitivity plots are shown in Fig. A3 (available online). We discuss some of the noteworthy non-detections below.

2MASS J01033203+1935361 – 2M0103+19 has been assigned β and INT-G gravity classifications (Kirkpatrick et al. 2000; Faherty et al. 2012; Allers & Liu 2013), however has not been assigned membership of a young moving group. Metchev et al. (2015) obtained 21 h of *Spitzer* monitoring, detecting variability in both the 3.6 and 4.5 μm bands. 2M0103+19 was observed to exhibit a regular periodic modulation with a period of 2.7 ± 0.1 h. This short rotational period combined with variability amplitudes of 0.56 ± 0.03 per cent and 0.98 ± 0.09 per cent in the 3.6 and 4.5 μm bands, respectively, would suggest that a *J*-band detection is likely for this object. Our observation taken on 2014 November 3 shows no evidence of variability over a 5.3 h observation. According to the sensitivity plot shown in Fig. A3 (available online), we would have detected variability with an amplitude > 2 per cent for a 2.7 h period with a 90 per cent probability.

GU Psc b – GU Psc b is a wide separation T3.5 planetary-mass companion to the young M3 star, a likely member of the AB Doradus moving group (Naud et al. 2014). Recently, Naud et al. (2017) reported results from a *J*-band search for variability in this object. Photometric variability with an amplitude of 4 ± 1 per cent was marginally detected during one ∼6 h observation, with no significant variations observed at two additional epochs. The authors estimate a period >6 h as the light curve does not appear to repeat during this observation. With a magnitude of $J = 18.12$, GU Psc b is ∼1 mag fainter than the other targets in our survey and we do not detect significant variability in its ∼3.5 h light curve. The sensitivity plot of GU Psc b presented in Fig. A3 (available online) shows that this observation is insensitive to variability with amplitudes < 10 per cent, and thus we cannot say whether the light curve has evolved from the variable epoch detected by Naud et al. (2017).

While this remains a prime target for variability monitoring, long observations and high photometric precision are needed to confirm and characterize its variability.

2MASS J16154255+4953211 – 2M1615+49 is identified as a young object by Cruz et al. (2007); Kirkpatrick et al. (2008), Allers & Liu (2013), although it has not been identified as a member of a young moving group. Kirkpatrick et al. (2008) tentatively assign this object an age estimate of ∼100 Myr based on its optical spectrum. Metchev et al. (2015) obtained 21 h of *Spitzer* 3.6 and 4.5 μm variability monitoring, finding significant variability in the 14 h 3.6 μm sequence but not in the 7 h 4.5 μm sequence. The authors estimate a period of ∼24 h for 2M1615+49. We do not observe any significant variability in our UKIRT *J*-band observation of 2M1615+49 taken on 2016 July 10. The sensitivity plot shown in Fig. A3 (available online) indicates that we are not sensitive to periods longer than ∼10 h, so it is unsurprising that we did not detect variability in this long-period variable.

HN Peg B – Discovered by Luhman et al. (2007), HN Peg B is a T2.5 dwarf companion to the 300 Myr old star HN Peg. Metchev et al. (2015) report significant variability in both the *Spitzer* 3.6 and 4.5 μm bands and estimate a period of ∼18 h. More recently, Zhou et al. (2018) obtained *HST* WFC3 near-IR monitoring of HN Peg B, observing significant variability at all wavelengths in the range 1.1–1.7 μm. They estimate a period of 15.4 ± 0.5 h and measure a *J*-band amplitude of 1.28 ± 0.3 per cent. We observed HN Peg B four times in total, twice with both the NTT and UKIRT telescopes, taking care to keep the primary HN Peg A off-frame. Although HN Peg A was kept off-frame for these observations, diffraction spikes still affected the quality of all of our observations. For our NTT data taken on 2014 October 8 and 2015 August 7, contaminated frames had to be removed from the light curve where the diffraction spikes coincided with the position of HN Peg B on the detector. For our UKIRT observations taken on 2016 July 11 and July 13 photometry from one nod position had to be removed from the data. Although the NTT light curves have lower σ_{pt}, their short duration (<2.5 h) means that they are insensitive to trends on time-scales >5 h. During two ∼5 h observations with UKIRT, we do not detect any significant variability. Longer duration observations will be needed to characterize the variability of this young companion.

8 ASSESSING EVIDENCE OF YOUTH IN THE SAMPLE

8.1 Analysing sample spectra

Our targets have been identified as potentially young in the literature, through indications of low gravity in their spectra and/or identification as probable members of young moving groups (e.g. Cruz et al. 2009; Allers & Liu 2013; Gagné et al. 2015a; Best et al. 2015). In this section, we consider gravity-sensitive features in the spectra of our targets. Kirkpatrick (2005) present a spectral classification scheme for L0–L5 brown dwarfs that includes three gravity classes based on gravity sensitive features in their optical spectra. The three gravity subtypes α, β, and γ, denote objects of normal gravity, intermediate gravity, and very low gravity, respectively. The δ suffix is used to designate objects with an even younger age (typically less than a few Myr) and lower surface gravity than those associated with the γ suffix (Kirkpatrick et al. 2006). Gagné et al. (2015a) use optically anchored IR spectral average templates for classifying the gravity subtype for L0–L9 dwarfs. This method assigns α, β, and γ subtypes for each object. Allers & Liu (2013) present an index-based infrared gravity classification method that is

based on FeH, VO, K I, Na I, and *H*-band continuum shape in the IR. A score of 0 indicates that the feature is consistent with field gravity objects, 1 indicates intermediate gravity, and 2 indicates very low gravity. A score of 'n' is assigned if either the spectrum does not cover the wavelength range of the index or the feature is not gravity-sensitive at the object's spectral type. A score of '?' indicates that an index hints at low gravity, but the uncertainty in the calculated index is too large. The final gravity classification (FLD-G, INT-G, VL-G) is assigned based on the median of the individual gravity scores, ignoring 'n' or '?' scores.

We present the spectral types, gravity subtypes, and the specific signatures of low gravity exhibited by each object in the sample in Table 3.

8.2 Assessing group membership

Following a similar method to Faherty et al. (2016), we investigate the likelihood that each object in the survey is a member of a young moving group using four methods of assessing group membership using kinematic data; the convergent point analysis of Rodriguez et al. (2013), the BANYAN I tool of Malo et al. (2013), the BANYAN Σ method in Gagné et al. (2018b), and the LACEwING analysis of Riedel et al. (2017).

Convergent point analysis estimates the probability of membership using the perpendicular motion of the candidate member and the convergent point location of a given moving group, but does not take into account radial velocity or parallax. This method considers six potential moving groups: TWA, THA, β Pic, AB Dor, CarN, and Col. BANYAN I uses a Bayesian statistical analysis to identify members of kinematic groups. BANYAN I minimally requires the position, proper motion, magnitude and colour of a star but radial velocity and distance measurements can be added. In addition to the groups considered by the convergent point analysis of Rodriguez et al. (2013), BANYAN I investigates membership in the Argus association. BANYAN Σ is a new Bayesian algorithm for identifying members of young moving groups that includes 27 young associations. This algorithm improves upon BANYAN I and II (Malo et al. 2013; Gagné et al. 2014a) by using analytical solutions when marginalizing over radial velocity and distance, using multivariate Gaussian models for the young moving groups and removing several approximations in the calculation of Bayesian likelihood. BANYAN Σ does not include the Argus association in its analysis, as it is likely that this association suffers from a high level of contamination (Bell et al. 2015). Proper motions, radial velocities and parallaxes used in this analysis are shown in Table 4

The results of each membership tool should be evaluated differently. Malo et al. (2013) and Gagné et al. (2018b) use a threshold of 90 per cent to confirm membership for the BANYAN I and Σ tools, respectively. We use this threshold probability of 90 per cent for the Convergent Point tool (Rodriguez et al. 2013). Riedel et al. (2017) find that a membership probability > 66 per cent indicates a high membership likelihood using LACEwING.

We present the results of each method in Table 5. To assess the membership probability of each object based on the results of the kinematic analysis, we use the categories outlined in Faherty et al. (2016):

(i) *Non-member* (NM): An object that is rejected from nearby associations due to its kinematics.

(ii) *Ambiguous member* (AM): An object requiring higher precision kinematics because it is classified as a candidate to more than one group or cannot be differentiated from field objects.

(iii) *High-likelihood member* (HLM): An object that does not have full kinematic information (proper motion, radial velocity, and parallax) but is regarded as high confidence (> 90 per cent for BANYAN I, BANYAN Σ, and Convergent Point analysis, > 66 per cent in LACEwING) in at least three out of four algorithms.

(iv) *Bona fide member* (BM): An object regarded as a high-likelihood member with full kinematic information.

Faherty et al. (2016) carried out this analysis on a larger sample of potential young objects, using Convergent Point analysis, BANYAN I, BANYAN II, and LACEwING. Our results, which substitutes BANYAN Σ for BANYAN II, are mostly consistent with those found in Faherty et al. (2016) with a few exceptions. 2M0303−73 drops from an ambiguous member of Tucana-Horologium in Faherty et al. (2016) to a non-member in our analysis. 2M0045+16 had been previously identified as a bona fide member of Argus (Faherty et al. 2016), however given the uncertainty in the Argus group, Gagné et al. (2018b) excluded this group from the analysis. The convergent point method and LACEwING assign it to the Argus association while BANYAN I and Σ assign it to the Carina-Near association. The object 2M0117−34 drops from a high-likelihood member to an ambiguous member. Compared to analysis in Faherty et al. (2016), we include a parallax measurement from Liu et al. (2016) for this object. All moving group tools favour the Tucana-Horologium association, however BANYAN Σ and LACEwING probabilities are below 90 per cent and 66 per cent, respectively. 2M0323−46, 2M0342−68, and 2M2322−61 all drop from a high-likelihood member to an ambiguous member due to lower membership probabilities calculated in BANYAN Σ compared to BANYAN II. 2M0326−21 is classified as an ambiguous member of AB Doradus because the Convergent Point tool and LACEwING predict membership probabilities of 66 per cent and 55 per cent, respectively. As can be seen in Table 5, our sample is composed of 6 bona fide members, 2 high-likelihood members, 24 ambiguous candidates, and 3 non-members.

We additionally look at our sample on a colour–magnitude diagram to check that they follow the general trends seen in intermediate and low-gravity objects to date (Faherty et al. 2016; Liu et al. 2016). Many objects in the sample have measured parallaxes from Dupuy & Liu (2012), Faherty et al. (2012, 2016), and Liu et al. (2016). When parallaxes were not available we used their estimated distance from kinematic group membership. We plot absolute magnitude against colour in Fig. 6. Overall, the survey objects appear redder and more luminous than the field brown dwarf population, as seen in a larger sample of young objects by Liu et al. (2016). However the object PSO 071.8–12, shown by red circle in Fig. 6, appears to be an outlier in this sequence. PSO 071.8–12 was discovered by Best et al. (2015), who find that it is a high-probability candidate of β Pictoris using BANYAN II. However, our group membership assigns PSO 071.8–12 a moderate probability candidacy of the AB Doradus moving group, with very low probability candidacy to β Pictoris. The estimated kinematic distance of 45 ± 7 pc assuming AB Doradus membership results in an absolute magnitude that is ~1 mag brighter than both T-type field brown dwarfs and T-type low-gravity objects. This overluminosity could be explained is PSO 071.8–12 is a binary, however Best et al. (2015) do not identify PSO 071.8–12 as a possible binary based on its spectrum. If PSO 071.8–12 is not a binary then we estimate that PSO 071.8–12 must lie at a distance of ~20−30 pc, and thus is not a member of AB Doradus. Intriguingly, β Pic membership would imply a distance of 19 ± 4 pc according to BANYAN Σ, which would result in

Table 3. Signatures of youth in sample.

Name	SpT (Opt)	Ref	SpT (IR)	Ref	K05 Class	K05 Ref	AL13 Ind	AL13 Class	AL13 Ref	Signs of youth[a]	Ref
2MASS J00011217+1535355	–	–	L4	G15a	β	G15a	1211	INT-G	G15a	OTR	G15a
2MASS J00452143+1634446	L2	C09	L2	AL13	β	G14a	1221	VL-G	AL13	OITRH	G14a
2MASS J01033203+1935361	L6	F12	L6	M03	β	G14a	1n11	INT-G	AL13	OITR	G14a
GU Psc b	–	–	T3.5	N14	–	N14	–	–	–	RM	N14
2MASS J01174748−3403258	L2	C03	L1	AL13	γ	G14a	1121	INT-G	AL13	TRM	G14a
2MASS J02340093−6442068	L0	K10	L0	F16	γ	G14a	2211	VL-G	F16	OR	G14a
2MASS J03032042−7312300	L2	K10	–	–	γ	G14a	–	–	–	OR	G14a
2MASS J03101401−2756452	L5	C07	–	–	γ	G14a	–	–	–	RHL	G14a
2MASS J03231002−4631237	L0	C09	L0	F16	γ	G14a	2222	VL-G	F16	ORL	G14a
2MASS J03264225−2102057	L5	G15a	L5	F16	β/γ	G15a	0n01	FLD-G	F16	RL	G14a
2MASS J03421621−6817321	L4	G15a	–	–	γ	G15a	–	–	–	R	G15a
PSO J057.2893+15.2433	–	–	L7	B15	–	B15	–	–	–	R	B15
2MASS J03552337+1133437	L5	C09	L3	AL13	γ	G14a	2122	VL-G	G15a	OITRL	G14a
2MASS J03572695−4417305	M9 + L1.5	M06	–	–	β	G14a	–	–	–	OR	G14a
2MASS J04185879−4507413	–	–	L3	G15a	γ	G15a	2211	VL-G	G15a	OR	G15a
2MASS J04210718−6306022	L5	C09	L5	F16	γ	G14a	0n11	INT-G	F16	OIRL	G14a
PSO J071.8769−12.2713	–	–	T2	B15	–	B15	–	–	–	–	–
2MASS J05012406−0010452	L4	C09	L3	AL13	γ	G14a	2112	VL-G	AL13	OTRL	G14a
2MASS J05120636−2949540	L5	K08	L5	G15a	β	G15a	1n01	INT-G	G15a	R	G15a
2MASS J05184616−2756457	L1	C07	L1	AL13	γ	G15a	2222	VL-G	AL13	OITRU	G14a
2MASS J05361998−1920396	L2	C07	L2	AL13	γ	G14a	2212	VL-G	AL13	OTR	G14a
SDSS J111010.01+011613.1	–		T5.5	G15c		G15c	–	–	–	MR	G15c
2MASS J12074836−3900043	L0	G14b	L1	G14b	δ	G15a	2222	VL-G	G15a	OITR	G15a
2MASS J12563961−2718455	–	–	L4	AL13	β	G15a	2021	VL-G	G15a	TR	G15a
2MASS J14252798−3650229	L3	R08	L4	G15a	γ	G15a	11?1	INT-G	G15a	TR	G15a
2MASS J16154255+4953211	L4	C07	L3	AL13	γ	G15a	2022	VL-G	AL13	OITRL	G14a
WISE J174102.78−464225.5	–	–	L7	S14	γ	S14	–	–	–	ITRM	S14
PSO J272.4689−04.8036	–	–	T1	B15	–	B15	–	–	–	–	–
2MASS J20025073−0521524	L6	C07	L5-7	G15a	γ	G15a	–	–	F16	–	–
2MASS J20113196−5048112	–	–	L3	G15a	γ	G15a	2222	VL-G	G15a	OT	G15a
PSO J318.5338−22.8603	–	–	L7	L13	γ	G15a	XXX2, 2X21	VL-G	L13	ITRM	G14a
2MASS J21324036+1029494	–	–	L4		β	G15a	00?1	FLD-G	G15a	TR	G15a
HN Peg B	–	–	T2.5	L07	–	L07	–	–	–	I	L07
SIMP J215434.5−105530.8	L4	G14c	L5	F16	β	G14c	0n11	INT-G	G15a	ITR	G15a
2MASS J2244316+204343	L6.5	K08	L6	AL13	γ	G15a	2n21	VL-G	AL13	ITRLM	G14a
2MASS J23225299−6151275	L2	C09	L3	F16	γ	G14a	1221	VL-G	G15a	OR	G14a

Note. References: AL13: Allers & Liu (2013), B15: Best et al. (2015), C03: Cruz et al. (2003), C07: Cruz et al. (2007), C09: Cruz, Kirkpatrick & Burgasser (2009), F12: Faherty et al. (2012), F16: Faherty et al. (2016), G14a: Gagné et al. (2014a), G14b: Gagné et al. (2014b), G14c: Gagné et al. (2014c), G15b Gagné et al. (2015c), G15c: Gagné et al. (2015a), K05: Kirkpatrick (2005), K08: Kirkpatrick et al. (2008), K10: Kirkpatrick et al. (2010), L13: Liu et al. (2013), M03: McLean et al. (2003), M06: Martín et al. (2006), N14: Naud et al. (2014), L07: Luhman et al. (2007), R08: Reid et al. (2008), S14 Schneider et al. (2014).

[a]A capital letter means the object displays the associated sign of youth. O: lower-than-normal equivalent width of atomic species in the optical spectrum, I: same but in the NIR spectrum, T: a triangular-shaped *H*-band continuum, R: redder-than-normal colours for given spectral type, U: over luminous, H: Hα emission, L: Li absorption, M: signs of low gravity from atmospheric models fitting.

magnitudes consistent with other T dwarfs. More kinematic data is needed to robustly assess the binarity and youth of PSO 071.8–12.

Combining the available kinematic information and spectral information for each target in the survey, we make a final call on whether the objects presented in Tables 3 and 5 are likely low gravity. We exclude three objects from the original survey on the basis that there is insufficient evidence of youth. These objects are classified as 'Uncertain' in Table 5. We discuss the excluded objects below. The object PSO 057.2+15 is excluded from the survey. This L7 object appears redder than the field population and exhibits a triangular shaped *H* band, however a gravity class could not be determined due to its low S/N spectrum (Best et al. 2015). The moving group tools suggest possible membership in AB Doradus or β Pictoris but are not consistent with each other. Updated kinematics and/or spectral analysis are needed to confirm the possible youth of this object. We thus exclude PSO 057.2+15 from the 'Young' sample. PSO 272.4–04 is a low-probability AB Doradus member using 3/4 membership tools. Gravity sensitive indices only

apply to objects with spectral types ≥L7, since low-gravity spectral signatures are not very well established for late-L and T-type objects. Thus, signatures of youth for the T1 objects PSO 272.4–04 could not be analysed (Best et al. 2015). We thus exclude it from the 'Young' sample. Gravity indices could not be analysed for the T2 object PSO 071.8–22 for the same reason. PSO 071.8–12 also has uncertain membership status, as discussed above, and we thus exclude it from the final statistical analysis of the survey. We additionally exclude the binary 2M0357–44 from the final survey. Although 2M0357–44 is likely young (Cruz et al. 2009; Gagné et al. 2015b), we have a reduced likelihood of detecting variability in either component of the binary, since the non-variable component would effectively dilute the variability signal. 2M2322–61 and 2M0412–63 are also left out of the survey because they were observed during poor weather conditions which prohibited us from determining meaningful constraints on their variability properties. Their light curves are shown in Fig. A2 (available online). In total we exclude six objects that we observed in our survey from the final

Table 4. Kinematic information of variability sample.

Name	$\mu_\alpha \cos\delta$	μ_δ	Ref	RV	Ref	π	Ref
2M0001+15	135.2 ± 10.7	− 169.6 ± 13.7	F16	–	–	–	–
2M0045+16	355 ± 10	− 40 ± 10	F16	3.16 ± 0.83	F16	65.9 ± 1.3	L16
2M0103+19	293.0 ± 4.6	27.7 ± 4.7	F12	–	–	46.9 ± 7.6	F12
GU Psc b	90 ± 6	− 102 ± 6	N14	− 1.6 ± 0.4	N14	–	–
2M0117−34	84 ± 15	− 45 ± 8	F16	(3.96 ± 2.09)	F16	26.1 ± 1.9	L16
2M0234−64	88 ± 12	− 15 ± 12	F16	11.762 ± 0.721	F16	(21 ± 5)	F16
2M0303−73	43 ± 12	3 ± 12	F16	–	–	–	–
2M0310−27	− 119 ± 18	− 47 ± 16	C08	–	–	–	–
2M0323−46	66 ± 8	1 ± 16	F16	13.001 ± 0.045	F16	(17 ± 3)	F16
2M0326−21	108 ± 14	− 146 ± 15	F16	(22.91 ± 2.07)	F16	(41 ± 1)	F16
2M0342−68	65.3 ± 2.8	18.5 ± 9.1	F16	(13.87 ± 2.62)	F16	(21 ± 9)	F16
PSO 057.2+15	68 ± 11	− 127 ± 12	B15	–	–	–	–
2M0355+11	225 ± 13.2	− 630 ± 15	F16	11.92 ± 0.22	F16	109.5 ± 1.4	F16
2M0357−44	64 ± 13	− 20 ± 19	F16	10.73 ± 4.6	F16	–	–
2M0418−45	53.3 ± 8.4	− 8.2 ± 12.6	F16	–	–	–	–
2M0421−63	146 ± 8	191 ± 18	F16	14.7 ± 0.33	F16	–	–
PSO 071.8−12	20 ± 19	− 89 ± 19	B15	–	–	–	–
2M0501−00	190.3 ± 9.5	− 142.8 ± 12.5	F16	21.77 ± 0.66	F16	48.4 ± 1.4	F16
2M0512−29	− 10 ± 13	80 ± 15	F16	–	–	–	–
2M0518−27	28.6 ± 4.2	− 16 ± 4	F16	24.35 ± 0.19	F16	18.4 ± 1.1	F16
2M0536−19	24.6 ± 5.3	− 30.6 ± 5	F16	22.065 ± 0.695	F16	21.1 ± 1.6	F16
SDSS 1110+0	− 217.1 ± 0.7	− 280.9 ± 0.6	G15a	7.5 ± 3.8	G15a	52.1 ± 1.2	D12
2M1207−39	− 57.2 ± 7.9	− 24.8 ± 10.5	F16	(9.48 ± 1.91)	F16	(15 ± 3)	F16
2M1256−27	− 67.4 ± 10.2	− 56.5 ± 12.7	F16	–	–	–	–
2M1425−36	− 284.89 ± 1.4	− 463.08 ± 1	F16	5.37 ± 0.25	F16	86.45 ± 0.83	F16
2M1615+49	− 80 ± 12	− 18 ± 12	F16	− 25.59 ± 3.18	F16	32 ± 1	L16
WISE 1741−46	− 20.4 ± 9.2	− 343 ± 13.7	F16	− 5.7 ± 5.1	F16	–	–
PSO 272.4−04	− 46 ± 4	− 400 ± 13	B15	–	–	–	–
2M2002−05	− 98 ± 5	− 110 ± 8	F16	–	–	–	–
2M2011−50	21.3 ± 8.1	− 71.3 ± 14.5	F16	–	–	–	–
PSO 318.5−22	137.3 ± 1.3	− 138.7 ± 1.4	F16	− 6.0 ± 0.95	A16	45.1 ± 1.7	L16
2M2132+10	107.8 ± 16.4	29.7 ± 18.1	F16	–	–	–	–
HN Peg B	–	–	–	–	–	–	–
SIMP 2154−10	175 ± 12	9 ± 12	F16	–	–	32.6 ± 1.0	L16
2M2244+20	252 ± 14	− 214 ± 11	F16	− 16.0 ± 0.85	V17	58.7 ± 1.0	L16
2M2322−61	62 ± 10	85 ± 9	F16	6.747 ± 0.75	F16	(22 ± 1)	F16

Note. References: C08: Casewell, Jameson & Burleigh (2008), D12: Dupuy & Liu (2012), G15a: Gagné et al. (2015c), F12: Faherty et al. (2012), F16: Faherty et al. (2016), N14: Naud et al. (2014), V17: Vos, Allers & Biller (2017).

sample of 30 young, low-gravity objects used in our analysis. We show the distribution of spectral types in our 30 object sample in Fig. 7.

9 VARIABILITY STATISTICS

Fig. 8 shows the spectral type of our sample plotted against $(J − K)_{2MASS}$ colour. Blue symbols correspond to variability detections, where the symbol size is proportional to the variability amplitude. Although many of our measured variability amplitudes are only a lower limit estimate, we see evidence for increasing *J*-band amplitude along the L sequence, something that is noted in Metchev et al. (2015) for mid-IR variability in field dwarfs.

To explore the effect of low surface gravity on variability properties, we compare our results to the results of variability surveys of the field brown dwarf population reported by Radigan et al. (2014) and Radigan (2014). Our methods for determining variability significance are very similar to the methods presented by Radigan et al. (2014). In both papers, the significance of a variability detection is based on the Lomb–Scargle periodogram power. In Radigan et al. (2014), the 1 per cent FAP periodogram power is empirically increased in the same way as our analysis (Section 3.5). Furthermore,

the same method is used to create the sensitivity plots in both surveys – by injecting simulated sinusoidal signals into reference star light curves and measuring the recovery rates. Thus, the two surveys can be robustly compared.

We find that 6/30 (20 per cent) of objects in the full statistical sample exhibit significant variability, similar to the 9/57 (16 per cent) reported by Radigan et al. (2014) for a similar high-gravity sample of field dwarfs. However, with only three young objects with spectral types >L9 included in our sample, we are lacking in L/T transition and T spectral type objects compared to the Radigan et al. (2014) and Radigan (2014) samples and thus we cannot obtain a robust comparison between the low-gravity and high-gravity populations as a function of spectral type. We thus consider objects with spectral types of L0–L8.5 in both samples. We find that 6/27 of L0–L8.5 low-gravity objects appear variable while Radigan (2014) report 2/34 variables in the field brown dwarf sample of L0–L8.5 objects.

9.1 Statistical formalism

Our formalism for the statistical analysis of this survey is based on the method described in Lafreniere et al. (2007) and Vigan et al.

Table 5. Moving group membership probabilities.

Name	Convergence[a]	P (per cent)	BANYAN I	P (per cent)	BANYAN Σ	P (per cent)	LACEwING	P (per cent)	Mem[b]	Decision[c]
2M0001+15	AB Dor	43.2	AB Dor	99.04	AB Dor	76.0	AB Dor	46	AM	Young
2M0045+16	CarN	74.2	Arg	99.97	CarN	89.0	Argus	99	AM	Young
2M0103+19	CarN	15.7	Old	96	Field	76.1	βPic	44	AM	Young
Gu Psc b	ABDor	99.5	ABDor	99.88	ABDor	89	ABDor	82	BM	Young
2M0117−34	THA	99.6	THA	92.4	THA	79.3	THA	51	AM	Young
2M0234−64	THA	79.5	THA	99.99	THA	96.3	THA	86	HLM	Young
2M0303−73	THA	97.6	Old	92.5	FLD	99.9	None	0	NM	Young
2M0310−27	CarN	99.9	Old	100	FLD	99.9	None	0	AM	Young
2M0323−46	THA	92.1	THA	99.97	THA	51.2	THA	41	AM	Young
2M0326−21	ABDor	65.8	ABDor	99.37	ABDor	91.9	AB Dor	55	AM	Young
2M0342−68	THA	98.3	THA	98.4	THA	67.7	None	0	AM	Young
PSO 057.2+15	ABDor	82.4	βPic	65.19	ABDor	67.2	None	0	AM	Uncertain
2M0355+11	ABDor	17.5	ABDor	99.99	ABDor	99.9	AB Dor	100	BM	Young
2M0357−44	THA	62.1	THA	53.07	Field, THA	66.6, 17.5	THA	39	AM	Young
2M0418−45	ABDor	91.5	ABDor	64	ABDor	41.9	AB Dor	24	AM	Young
2M0421−63	βPic, CarN	95.8, 95.9	βPic	92.8	CarN	93.8	CarN	38	AM	Young
PSO 071.8−12	ABDor	77.8	ABDor	62.7	ABDor	56.5	Col	32	AM	Uncertain
2M0501−00	THA	98.7	Old	99.86	Field	99.9	AB Dor	70	AM	Young
2M0512−29	CarN	5.5	Old	89.49	Field	99.9	None	0	NM	Young
2M0518−27	CarN	22.1	Col	86.5	βPic	62.7	Col	77	AM	Young
2M0536−19	βPic	77.5	βPic	57.28	βPic	81.1	Col	52	AM	Young
SDSS1110+01	ABDor	17.2	ABDor	99.91	ABDor	99.3	AB Dor	46	BM	Young
2M1207−39	βPic, TWA	100, 91.6	TWA	99.14	TWA	91.6	TWA	98	HLM	Young
2M1256−27	ABDor	75.8	TWA	99.14	Field	99.8	None	0	AM	Young
2M1425−36	ABDor	39.3	ABDor	99.98	ABDor	99.7	AB Dor	100	BM	Young
2M1615+49	ABDor	59.3	ABDor	95.12	ABDor	84.0	AB Dor	68	AM	Young
WISE 1741−46	βPic, ABDor	94.1, 91.8	βPic	99.88	ABDor, βPic	52.7, 45.9	AB Dor	71	AM	Young
PSO 272.4−04	TWA	61.8	ABDor	86.45	ABDor	89.0	AB Dor	29	AM	Uncertain
2M2002−05	None	0	Old	100	Field	99.9	None	0	NM	Young
2M2011−50 2	Col	96.5	THA	66.53	Field	72.2	None	0	AM	Young
PSO 318.5−22	βPic	98.9	βPic	99.99	βPic	99.6	β Pic	69	BM	Young
2M2132+10	CarN	92.8	Arg	53.44	Field	99.9	None	0	AM	Young
HN Peg B	–	–	–	–	–	–	–	–	–	Young
SIMP 2154−10	CarN	28.8	Old	89.97	CarN	71.4	None		AM	Young
2M2244+20	ABDor	68.9	AB Dor	99.99	ABDor	99.8	AB Dor	100	BM	Young
2M2322−61	THA	34.1	THA	99.78	THA	79.7	THA	97	AM	Young

[a]Moving groups: AB Dor: AB Doradus, Arg: Argus, β Pic: β Pictoris, CarN: CarN, Col: Col, THA: Tucana-Horologium, TWA: TW Hydrae.
[b]BM: Bona fide member, HLM: high-likelihood member, AM: ambiguous member, NM: non-member.
[c]Final decision based on spectral signatures of youth, membership probabilities, and colour–magnitude diagrams. Young: Object is a high-likelihood member of a young moving group and/or has clear indications of youth in its IR and/or optical spectrum. Uncertain: This object does not have sufficient evidence of youth and is thus excluded from the final statistical sample.

(2012). We consider the observation of N targets enumerated by $j = 1 \ldots N$. We note f, the fraction of objects that exhibit variability with amplitude and rotational period in the interval $[a_{\min}, a_{\max}] \cap [r_{\min}, r_{\max}]$, and p_j, the probability that such variability would be detected from our observations. With this notation, the probability of detecting variability in target j is (fp_j) and the probability of not detecting variability is $(1 - fp_j)$. Denoting d_j the detections made by the observations, such that $d_j = 1$ for a variability detection in target j and 0 otherwise, the likelihood of the data given f is

$$L(d_j|f) = \prod_{j=1}^{N} (1 - fp_j)^{1-d_j} (fp_j)^{d_j}. \qquad (1)$$

According to Baye's theorem, from the a priori probability density $p(f)$, or prior distribution, and the likelihood function L, we can calculate the posterior distribution $p(f|d_j)$, the probability density updated in light of the data:

$$p(f|d_j) = \frac{L(d_j|f) p(f)}{\int_0^1 L(d_j|f) p(f) \mathrm{d}f}. \qquad (2)$$

This is the frequency of variable objects, or variability occurrence rate of objects in the survey.

9.2 Estimating the frequency of variable objects

We use a modified version of the Quick Multi-purpose Exoplanet Simulation System (QMESS; Bonavita, de Mooij & Jayawardhana 2013; Bonavita et al. 2016) to calculate the posterior distribution of the frequency of variable objects in the survey. QMESS is a grid-based, non-Monte Carlo simulation code that uses direct-imaging sensitivity plots to estimate the frequency of giant planets. We use QMESS to estimate the fraction of objects that display variability using the statistical framework discussed above. We use the sensitivity plots obtained for each observation (described in Section 5) as p_j in equation (1) to calculate the likelihood, L for values of f between 0 and 1. For the Radigan (2014) sample, we use the average sensitivity plot from the Radigan et al. (2014) survey. This is reasonable since the reported photometric precision and observation lengths are comparable for both surveys (Radigan 2014). Since we
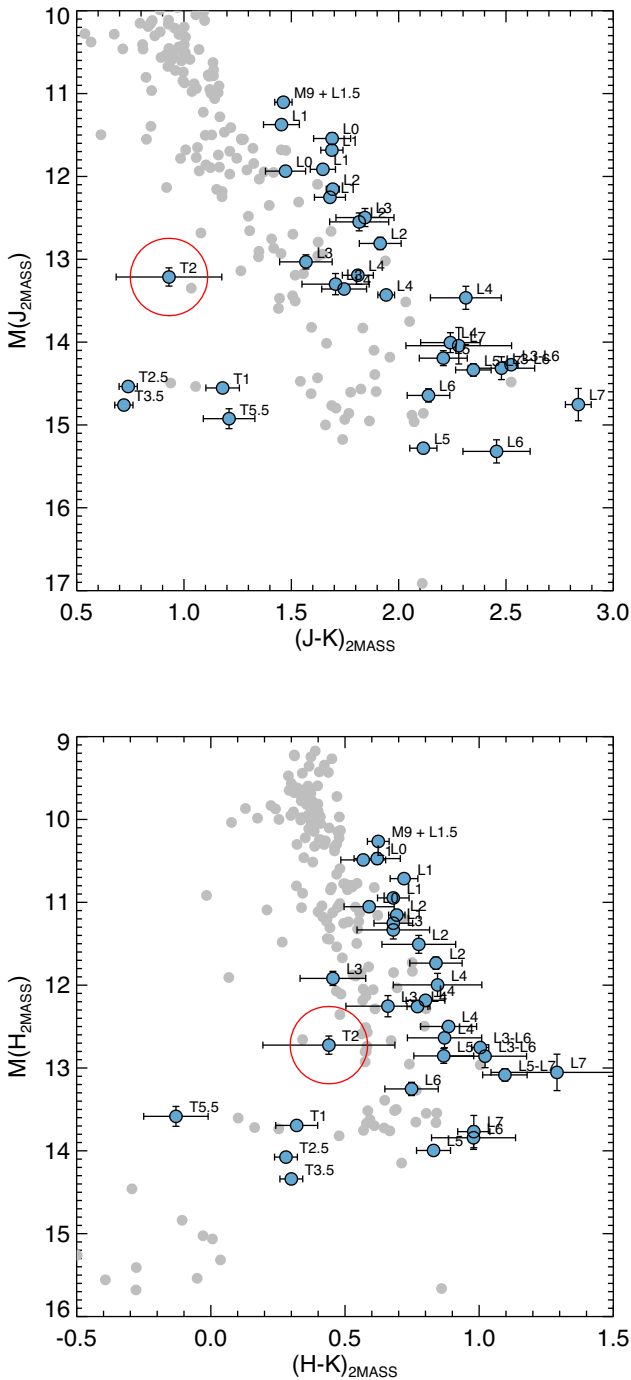
Figure 6. Colour–magnitude diagrams showing the field brown dwarf population (grey points) and our full sample of objects showing signs of low gravity. Absolute magnitudes were calculated either using measured parallaxes or kinematic distances. From this analysis it is clear that the T2 object PSO 071.8−12 (shown in red circle) is an outlier in the sample. Assuming AB Doradus membership for PSO 071.8−12 results in magnitudes that are ~1 mag brighter than other T dwarfs in the field and young populations.

have no prior knowledge of the variability frequency of low-gravity brown dwarfs, we use a uniform prior distribution of $p(f) = 1$ in equation (2) to calculate the posterior probability density, $p(f|d_j)$. This is the probability density function (PDF) of the frequency of variable objects. The PDFs of the frequency of variable objects for the 'Young' sample and field brown dwarf sample (Radigan 2014)
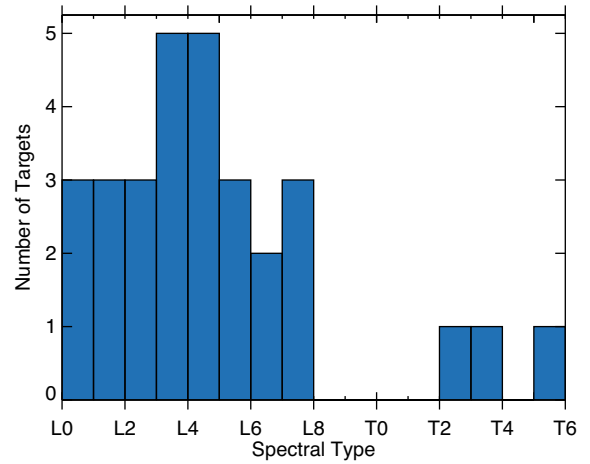
Figure 7. Histogram showing the distribution of spectral types in our final sample of 30 low-gravity brown dwarfs. Few young, low-gravity T dwarfs bright enough for variability observations are known, so our sample is predominantly composed of objects with spectral types <L8.5.
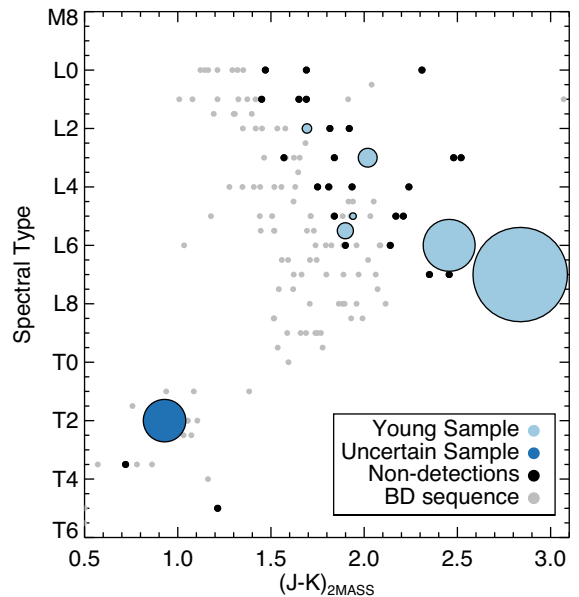
Figure 8. Spectral type of variable objects plotted against $(J − K)_{2MASS}$ colour. Blue symbols represent young objects displaying significant photometric variability, where the radius is proportional to the variability amplitude. Dark blue symbols denote the objects that are highly likely to be young while light blue circles denote objects whose youth is more uncertain.

are plotted in Figs 9 and 10. For the low-gravity sample analysed in this work, we find the frequency of variables objects is 30^{+16}_{-8} per cent, which is higher than the rate of 11^{+13}_{-4} per cent that we find for the Radigan (2014) survey.

We additionally employ a second method to analyse how statistically significant the correlation between low-gravity and frequent variability is. To do this we use a Bayesian framework to analyse the 2×2 contingency table shown in Table 6, following the method described by Biller et al. (2011) to determine the probability that the samples are drawn from different distributions. We denote y_1 as the number of young objects with detected variability and y_2 as the number of field objects with detected variability. We model the
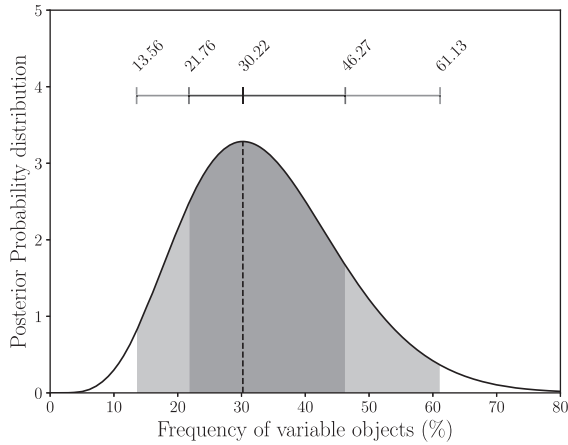
Figure 9. Probability distribution of the frequency of variable objects in the 'Young' sample. The dark grey area shows the 1σ regions while the light grey area shows the 3σ region.
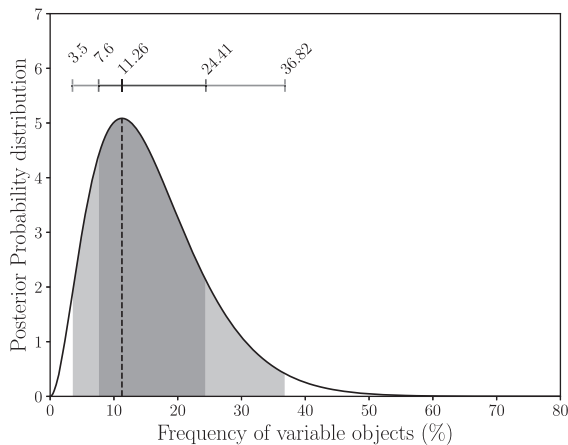
Figure 10. Probability distribution of the frequency of variable objects in the field brown dwarf sample (Radigan 2014). The dark grey area shows the 1σ regions while the light grey area shows the 3σ region.

Table 6. Contingency table showing the number of variability detections and non-detections in the Radigan (2014) survey (field objects) and this survey (low-gravity).

	Variable	Non-variable
Field objects	2	32
Low-gravity	6	21

number of variable objects as a binomial function:

$$y_1 \sim \mathrm{Binom}(n_1, \theta_1), \tag{3}$$

$$y_2 \sim \mathrm{Binom}(n_2, \theta_2), \tag{4}$$

where n_1, n_2 are the total sample sizes and θ_1, θ_2 are the variability occurrence rates of the low-gravity and field objects, respectively. We use uniform priors on the fraction of variable for each population:

$$\theta_1 \sim \mathrm{Unif}(0, 1) = \mathrm{Beta}(1, 1), \tag{5}$$

$$\theta_2 \sim \mathrm{Unif}(0, 1) = \mathrm{Beta}(1, 1). \tag{6}$$

Since the Beta distribution is a conjugate prior to the binomial distribution we can analytically compute the posteriors of the variability occurrence rate for each sample:

$$p(\theta_1|y_1, n_1) = \int_{-\infty}^{+\infty} \mathrm{Beta}(\theta_1|y_1 + 1, n_1 - y_1 + 1), \tag{7}$$

$$p(\theta_2|y_2, n_2) = \int_{-\infty}^{+\infty} \mathrm{Beta}(\theta_2|y_2 + 1, n_2 - y_2 + 1). \tag{8}$$
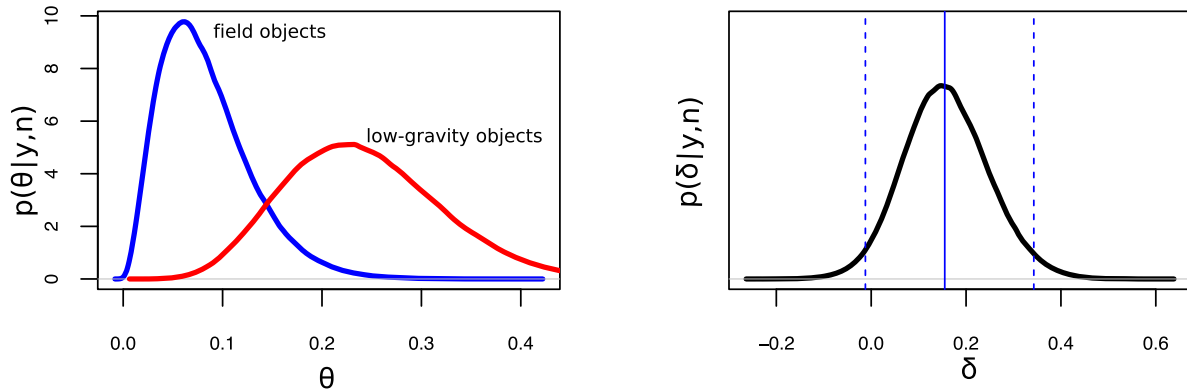
We plot the probability distributions of the variability occurrence rates in the left-hand panel of Fig. 11. We define the difference between the variability occurrence rates as $\delta = \theta_1 - \theta_2$. We then draw 10 000 simulations from the joint posterior $p(\theta_1, \theta_2|y_1, n_1, y_2, n_2)$ and estimate the probability that $\delta > 0$ by the fraction of samples, m, where $\theta_1^m > \theta_2^m$. We plot the distribution δ in the right-hand panel of Fig. 11. We find a 98 per cent probability that the variability occurrence rates of the field brown dwarf and low-gravity populations are drawn from different distributions. Thus, our survey strongly suggests that the low-gravity L-type objects appear more variable than their higher mass counterparts.

Due to a low number of young T dwarfs in our sample, our survey cannot place strong constraints on the variability properties of low-gravity T-type objects. However there are a number of high-amplitude variability detections in young T dwarfs that suggest that this trend between low-gravity and high-amplitude variability may extend into the T dwarfs. Metchev et al. (2015) report *Spitzer* 3.6 and 4.5 μm in the intermediate-gravity T2.5 companion HN Peg B, the only low-gravity T dwarf in the survey. The T2.5 known variable object SIMP 0136 was recently found to be a likely planetary-mass member of the Carina-Near moving group (Gagné et al. 2017). With its 1–6 per cent *J*-band variability, SIMP 0136 exhibits one of the highest variability amplitudes of the known variable T dwarfs. Gagné et al. (2018a) recently reported that the T2 object 2M1324+63 is a planetary-mass member of the AB Doradus moving group. This object is known to exhibit high-amplitude variability in the optical and the mid-IR (Heinze et al. 2015; Apai et al. 2017) and also provides a good spectrophotometric match to the directly imaged planet HR8799b (Bonnefoy et al. 2016). Finally, we report high-amplitude variability in PSO 071.8–22 in this survey. Although it does not have sufficient evidence of youth to be classed as 'Young' in our sample, additional kinematic information may confirm PSO 071.8–12 as a young object. As we identify more low-gravity T dwarfs it will become clearer whether the link between low-gravity and enhanced variability holds for cooler T-type objects.

10 FOLLOW-UP OBSERVATIONS OF VARIABLE OBJECTS

When possible, we obtained follow-up observations of objects found to be variable in their first epoch. These observations were carried out so that we could confirm variability and also look for evidence of light-curve evolution for our variable objects (Apai et al. 2017; Vos et al. 2018). We obtained follow-up observations of 2M0045+16, PSO 071.8–12, 2M0501–00, 2M1425–36, and PSO 318.5–22. We discuss each object below.

2M0045+16 – We observed 2M0045+16 on 2014 November 11 and 2015 August 17 with the NTT and 2016 November 13

Figure 11. Left-hand panel shows probability distributions for the variability occurrence rate of the field brown dwarf sample (blue) from Radigan et al. (2014) and the low-gravity sample (red) from this survey, assuming binomial statistics and a uniform prior. The right-hand panel shows the difference between these distributions. We find a 98 per cent probability that the planetary-mass sample has a higher variability occurence rate than the field brown dwarf sample.
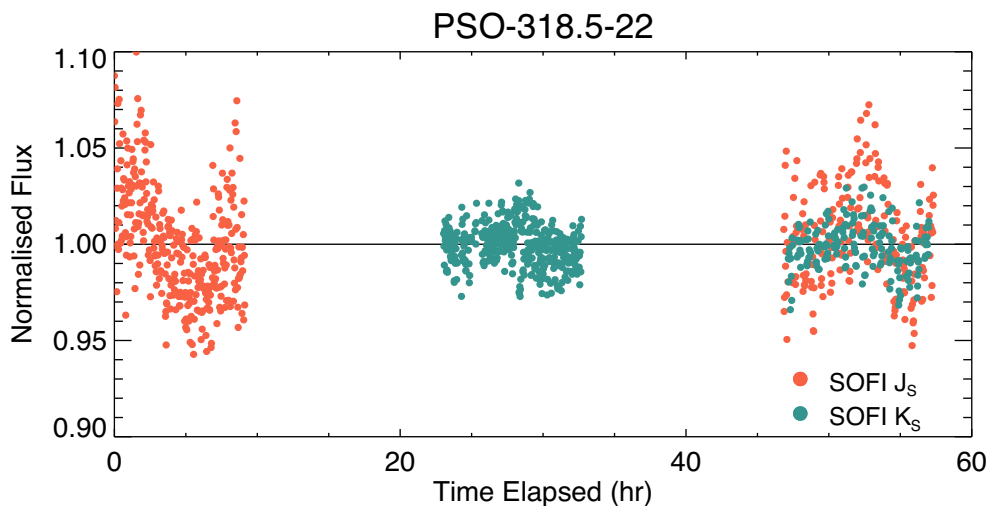

Figure 12. Follow-up observations of PSO 318.5–22 taken over three consecutive nights. Orange points show observations taken with the J_S filter and the teal points show the K_S filter observation. These three nights allow us to constrain the rotational period of PSO 318.5–22 to ∼8.5 h, in agreement with the 8.6 h period reported by Biller et al. (2018).

with UKIRT. 2M0045+16 was found to be variable in two out of three epochs – the NTT 2014 November 11 and UKIRT 2016 November 13 observation. As can be seen from the sensitivity plots in Fig. 5, both light curves exhibit a similar shape, with periodograms indicating a period of ∼3−6 h. We measure amplitudes of 1.0 ± 0.1 per cent and 0.9 ± 0.1 per cent for the 2014 and 2016 light curves, respectively, thus we do not see any indication of light-curve evolution in this case. The NTT 2015 August 17 light curve shows a similar trend, however the periodogram peak power does not fall above our significance threshold. According to the sensitivity plot of the 2015 August 17 observation (shown in Fig. A3 which is available online), we can place an upper limit on the variability amplitude of this epoch of ∼2 per cent for a rotational period of ∼3−6 h. Thus, we did not reach the photometric precision necessary to robustly detect a 1 per cent modulation in the light curve in this observation.

PSO 071.8–12 – We reobserved the variable object PSO 071.8–12 with UKIRT on 2017 December 8. During this 4 h observation we do not detect significant variability. The sensitivity plot shown in Fig. A3 (available online) rules out significant variability > 5 per cent for short periods, however we believe that PSO 071.8–

12 has a somewhat longer period. For a rotational period of 5−8 h we place an upper limit of 6–8 per cent on the variability amplitude of PSO 071.8–12 in this epoch.

2M0501–00 – We observed 2M0501–00 a total of four times with the NTT. We detect significant variability on 2014 November 11 and 2016 October 19 and do not detect variability on 2015 August 16 and 2017 March 12. In the two variable epochs (Figs 4 and 5), which are separated by almost 2 yr we observe a similar light-curve shape – a slowly decreasing relative flux over the entire observation. Both periodograms favour a period >5 h and the Levenberg–Marquardt least-squares fits give amplitudes of 1–2 per cent, although both the rotational period and variability amplitude are very uncertain since we did not observe a maximum or minimum in either light curve. We do not detect variability during two ∼2 h observations on 2015 August 16 and 2017 March 12 (shown in Fig. A3; available online). As these observations are shorter than the variable epochs, they are less sensitive to long-period variability. The sensitivity plot from 2015 August 16 shows that this observation is sensitive to amplitudes > 6 per cent for a rotational period of 5 h. The 2017 March 12 light curve is noisier than the other epochs due to poor weather conditions, and the sensitivity plot indicates that the observation is
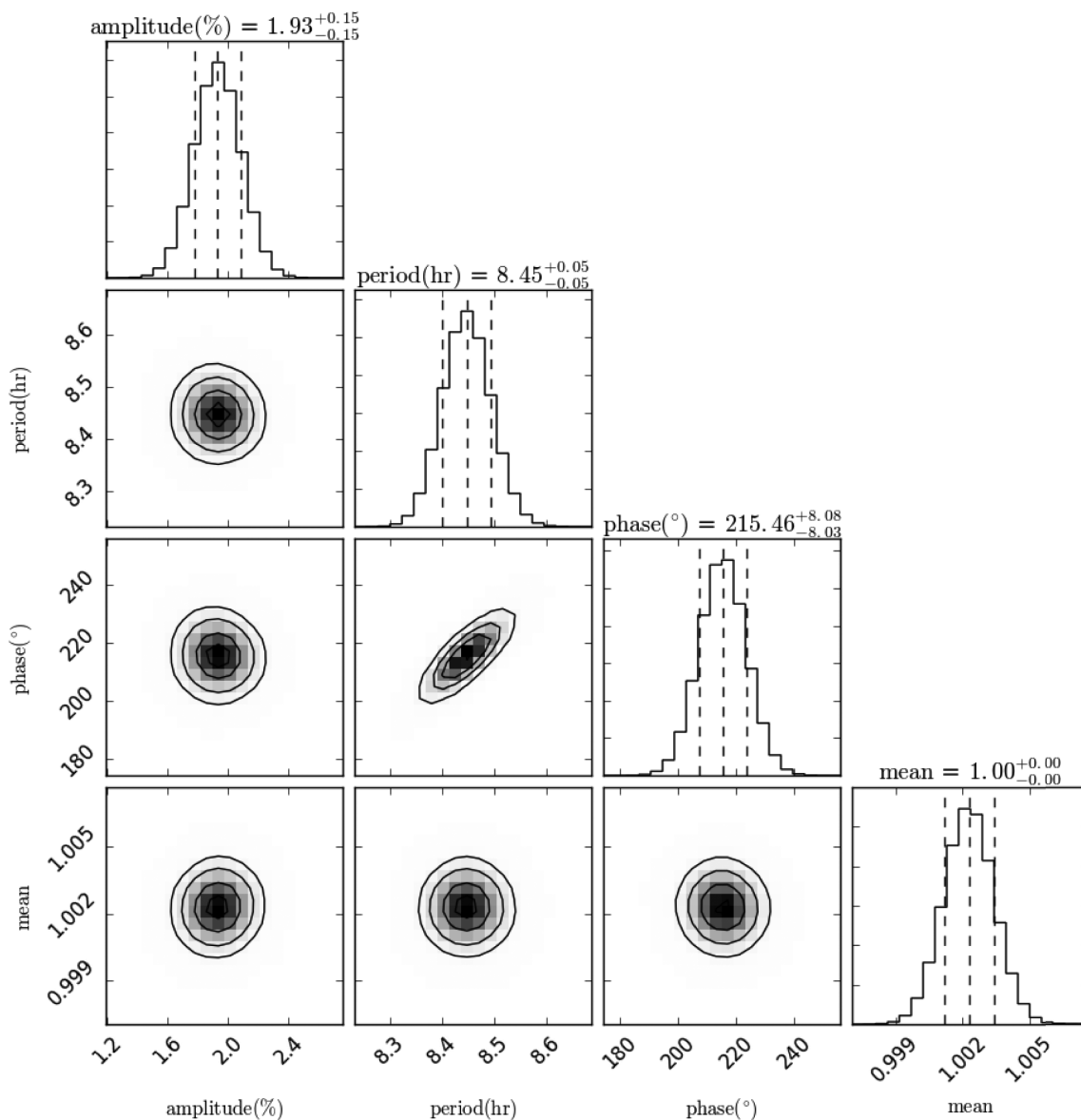
Figure 13. PSO 318.5–22 posterior distributions for amplitude, period, phase, and the mean obtained from MCMC analysis.

not sensitive to periods of ≥ 5 h in this epoch. Thus, our observations do not show evidence for an evolving light curve in this case.

2M1425–36 – We obtained two epochs of variability monitoring of 2M1425–36 with NTT/SofI. The initial observation on 2015 August 17 shows a low-amplitude ($\sim$0.7 per cent) trend with a period >2.5 h. Our second epoch observation, obtained using the NTT on 2017 March 14 (shown in Fig. A4; available online) suffered from poor weather conditions, with the seeing ranging from 0.9 to 1.7 arcsec. While the sensitivity plot suggests sensitivity to very low variability amplitudes, the periodograms of the reference stars display significant trends due to changing weather conditions.

PSO 318.5–22 – As part of the initial survey observations, we obtained three epochs of NTT variability monitoring for the L7 object PSO 318.5–22. On 2014 October 9 we observed significant J_S variability, with an amplitude of 10 ± 1.3 per cent, and a period >5 h (Fig. 5). The J_S light curve obtained on 2014 November 9 again shows similar variability, this time varying with an amplitude of 4.8 ± 0.7 per cent over a $\sim$3 h observation. Finally, we observed

PSO 318.5–22 in the K_S band on 2014 November 10. Since PSO 318.5–22 is much brighter in K_S, we attain higher photometric precision in this band. The light curve shows a smooth upward trend with an amplitude of 2.2 ± 0.6 per cent (Fig. 5). All three light curves were originally presented in Biller et al. (2015).

11 FOLLOW-UP OBSERVATIONS OF PSO 318.5–22

Additional observations of PSO 318.5–22 were taken in 2016 August, to more accurately constrain the rotational period and to investigate the wavelength dependence of the variability. On 2016 August 9, we observed using the J_S filter, followed by the K_S filter on 2016 August 10. Finally, on 2016 August 11, we observed with both filters, swapping over every 20 min. The data were reduced and analysed as described in Sections 3.1, 3.3, and 3.5. The corrected light curves for all three nights are shown in Fig. 12. We detect significant variability in both bands in all three epochs.

The J_S light curve obtained on 2016 August 9 shows significant variability with an amplitude of 2.4 ± 0.2 per cent. This is the highest amplitude detected over the course of the three nights but is much lower than the initial variability detection on 2014 October 9. This suggests that we are observing a quiescent phase of the variability of PSO 318.5–22, as has been observed previously in a number of variable brown dwarfs (Artigau et al. 2009; Radigan et al. 2012; Apai et al. 2017). The K_S light curve obtained on 2016 August 10 also shows significant variability. We fit a sinusoid to the light curve to obtain a variability amplitude of 0.48 ± 0.08 per cent.

The simultaneous J_S and K_S monitoring obtained on 2016 August 11 allows us to directly compare the variability in both bands during a single rotational phase. We observe significant variability in both filters and we measure a A_K/A_J ratio of 0.36 ± 0.25. This is similar to the ratios previously observed for the population of field brown dwarfs (Artigau et al. 2009; Radigan et al. 2012), suggesting that the variability mechanism for the exoplanet analogues is similar to that of the field brown dwarfs. Biller et al. (2018) obtained simultaneous *HST* WFC3 and *Spitzer* IRAC variability monitoring of PSO 318.5–22, detecting variability amplitudes of ∼3 per cent in the *Spitzer* 3.6 μm band and ∼4–6 per cent in the near-IR bands (1.07–1.67 μm). The variability amplitude was found to decrease with increasing wavelength and we observe this same trend with the high J_S amplitude and lower K_S amplitude.

Additionally, we find that the J_S and K_S variability is in phase. Biller et al. (2018) report large phase shifts between the near-IR and mid-IR light curves of PSO 318.5–22, and tentative phase shifts between the near-IR spectral bands. Phase changes have been attributed to different wavelengths probing different heights in the atmosphere (Buenzli et al. 2012; Biller et al. 2013), so this suggests that the J_S and K_S bands probe similar heights in the photosphere, while the mid-IR band is sensitive to surface homogeneities that are located at higher atmospheric levels.

The long baseline of this observation allows us to constrain the rotational period of PSO J318.5–22 using Monte Carlo analysis. We use the EMCEE package (Foreman-Mackey et al. 2013) to obtain the full posterior probability distributions for each parameter of the sinusoidal model. We use 500 walkers with 20 000 steps and discard an initial burn-in sample of 1000 steps to explore the four-dimensional parameter space to model the light curve. Fig. 13 shows the posterior distributions of the amplitude, period, phase and constant parameters of the fit. Each parameter is well constrained, and the MCMC method gives a rotational period of 8.45 ± 0.05 h for PSO J318.5–22. The derived error of 0.05 h on the period is very small, which shows the advantage of having long temporal coverage. However it is important to keep in mind that the above fit assumes a sinusoidal model that did not change between nights, and in reality the full light curve may resemble a more complex or evolving function. In any case, our estimated rotational period is consistent with the 8.6 ± 0.1 h period reported by Biller et al. (2018) using 16 h of *Spitzer* monitoring. This further supports our choice of a sinusoidal model and the derived posterior parameters.

12 CONCLUSIONS

We report the first large survey for photometric variability in young low-gravity brown dwarfs with NTT/SofI and UKIRT/WFCAM. We monitored a total of 36 objects continuously for ∼2−6 h, detecting significant ($p > 99$ per cent) variability in seven objects. We assess the spectral indicators of youth and moving group membership of each object in the sample, finding that three objects have rather uncertain ages and are thus left out of the survey analysis.

We also leave one unresolved binary out of the survey and lose two objects due to poor weather conditions. We detect variability in six objects that are likely to be young, four of which are new detections of variability.

In the 'Young' sample, we detect variability in 6/30 (20 per cent) objects, which is consistent with the 16 per cent variability fraction reported by Radigan et al. (2014) for the higher mass, field dwarfs. However, since we are lacking in objects with spectral types >L9 compared to earlier surveys of field L and T dwarf population, we focus our analysis on the L0–L8.5 objects in our sample. We find that the frequency of variable L0–L8.5 objects in this survey is 30^{+16}_{-8} per cent, which is higher than the frequency of variable objects of 11^{+13}_{-4} per cent that we find for the field brown dwarf population (Radigan 2014). We find that the PDFs of the variability occurrence rates of our two samples are drawn from different underlying distributions with a probability of 98 per cent. Thus, we have found the first quantitative indication that the L-type low-gravity objects are more likely to be variable than their higher mass field dwarf counterparts.

We additionally present three consecutive nights of photometric monitoring of the highly variable L7 spectral type object PSO 318.5–22 with NTT/SofI. We find no evidence of phase shifts between the J_S and K_S bands and find a A_K/A_J ratio of 0.36 ± 0.25, consistent with previous amplitude ratios of field brown dwarfs (Artigau et al. 2009; Radigan et al. 2012). This suggests that the underlying variability mechanism is the same for both populations. We perform MCMC analysis on the J_S light curves to measure a rotational period of 8.45 ± 0.05 h for PSO 318.5–22.

REFERENCES

Allers K. N., Liu M. C., 2013, ApJ, 772, 79
Allers K. N., Gallimore J. F., Liu M. C., Dupuy T. J., 2016, ApJ, 819, 133
Apai D., Radigan J., Buenzli E., Burrows A., Reid I. N., Jayawardhana R., 2013, ApJ, 768, 121
Apai D. et al., 2016, ApJ, 820, 40
Apai D. et al., 2017, Science, 357, 683
Artigau É., Bouchard S., Doyon R., Lafrenière D., 2009, ApJ, 701, 1534
Barenfeld S. A., Bubar E. J., Mamajek E. E., Young P. A., 2013, ApJ, 766, 6

Bell C. P. M., Mamajek E. E., Naylor T., 2015, MNRAS, 454, 593
Best W. M. J. et al., 2015, ApJ, 814, 118
Biller B. A., Allers K., Liu M. C., Close L. M., Dupuy T. J., 2011, ApJ, 730, 39
Biller B. A. et al., 2013, ApJ, 778, L10
Biller B. A. et al., 2015, ApJ, 813, L23
Biller B. A. et al., 2018, AJ, 155, 95
Bonavita M., de Mooij E. J. W., Jayawardhana R., 2013, PASP, 125, 849
Bonavita M., Desidera S., Thalmann C., Janson M., Vigan A., Chauvin G., Lannier J., 2016, A&A, 593, A38
Bonnefoy M. et al., 2016, A&A, 587, A58
Bouy H., Brandner W., Martı E. L., Delfosse X., Allard F., 2003, AJ, 1526
Buenzli E. et al., 2012, ApJ, 760, L31
Buenzli E., Apai D., Radigan J., Reid I. N., Flateau D., 2014, ApJ, 782, 77
Buenzli E., Saumon D., Marley M. S., Apai D., Radigan J., Bedin L. R., Reid I. N., Morley C. V., 2015, ApJ, 798, 127
Casali M. et al., 2007, A&A, 467, 777
Casewell S. L., Jameson R. F., Burleigh M. R., 2008, MNRAS, 390, 1517
Croll B., Muirhead P. S., Lichtman J., Han E., Dalba P. A., Radigan J., 2016, preprint (arXiv:1609.03587)
Cruz K. L., Reid I. N., Liebert J., Kirkpatrick J. D., Lowrance P. J., 2003, AJ, 126, 2421
Cruz K. L. et al., 2007, AJ, 133, 439
Cruz K. L., Kirkpatrick J. D., Burgasser A. J., 2009, AJ, 137, 3345
Dupuy T. J., Liu M. C., 2012, ApJS, 201, 19
Eriksson S., 2016, MSc thesis, Stockholm University. http://su.diva-portal.org/smash/record.jsf?pid = diva23A1178019&dswid = 2943
Faherty J. K. et al., 2012, ApJ, 752, 56
Faherty J. K. et al., 2016, ApJS, 225, 10
Foreman-Mackey D., Hogg D. W., Lang D., Goodman J., 2013, PASP, 125, 306
Gagné J., Lafrenière D., Doyon R., Malo L., Artigau É., 2014a, ApJ, 783, 121
Gagné J., Faherty J. K., Cruz K., Lafrenière D., Doyon R., Malo L., Artigau É., 2014b, ApJ, 785, L14
Gagné J., Lafrenière D., Doyon R., Artigau E., Malo L., Robert J., Nadeau D., 2014c, ApJ, 792
Gagné J. et al., 2015a, ApJS, 219, 33
Gagné J., Lafrenière D., Doyon R., Malo L., Artigau É., 2015b, ApJ, 798, 73
Gagné J., Burgasser A. J., Faherty J. K., Lafrenière D., Doyon R., Filippazzo J. C., Bowsher E., Nicholls C. P., 2015c, ApJ, 808, L20
Gagné J. et al., 2017, ApJ, 841, L1
Gagné J., Allers K. N., Theissen C. A., Faherty J. K., Gagliuffi D. B., Artigau É., 2018a, ApJ, 854, L27
Gagné J. et al., 2018b, ApJ, 856, 23
Gelino C. R., Marley M. S., Holtzman J. A., Ackerman A. S., Lodders K., 2002, ApJ, 577, 433
Heinze A. N., Metchev S., Kellogg K., 2015, ApJ, 801
Hodgkin S. T., Irwin M. J., Hewett P. C., Warren S. J., 2009, MNRAS, 394, 675
Irwin M. J. et al., 2004, in Quinn P. J., Bridger A., eds, Proc. SPIE Conf. Ser. Vol. 5493, Optimizing Scientific Return for Astronomy through Information Technologies. SPIE, Bellingham, p. 411
Irwin J., Hodgkin S., Aigrain S., Bouvier J., Hebb L., Moraux E., 2008, MNRAS, 383, 1588
Kirkpatrick J. D. et al., 2000, AJ, 120, 447
Kirkpatrick J. D., 2005, ARA&A, 43, 195
Kirkpatrick J. D., Barman T. S., Burgasser A. J., McGovern M. R., McLean I. S., Tinney C. G., Lowrance P. J., 2006, ApJ, 639, 1120
Kirkpatrick J. D. et al., 2008, ApJ, 689, 1295
Kirkpatrick J. D. et al., 2010, ApJS, 190, 100
Lafreniere D. et al., 2007, ApJ, 670, 1367
Lew B. W. P. et al., 2016, ApJ, 829, L32
Liu M. C. et al., 2013, ApJ, 777, L20
Liu M. C., Dupuy T. J., Allers K. N., 2016, ApJ, 833, 96
Luhman K. L. et al., 2007, ApJ, 654, 570

Malo L., Doyon R., Lafrenière D., Artigau É., Gagné J., Baron F., Riedel A., 2013, ApJ, 762, 88
Mamajek E. E., Bell C. P. M., 2014, MNRAS, 445, 2169
Manjavacas E. et al., 2018, AJ, 155, 11
Martín E. L., Brandner W., Bouy H., Basri G., Davis J., Deshpande R., Montgomery M. M., 2006, A&A, 456, 253
McLean I. S., McGovern M. R., Burgasser A. J., Kirkpatrick J. D., Prato L., Kim S. S., 2003, ApJ, 596, 561
Metchev S. A. et al., 2015, ApJ, 799, 154
Miles-Páez P. A., Metchev S. A., Heinze A., Apai D., 2017, ApJ, 840, 83
Morales-Calderon M. et al., 2006, ApJ, 43, 544
Mortier A., Faria J. P., Correia C. M., Santerne A., Santos N. C., 2015, 101, 1
Naud M.-E. et al., 2014, ApJ, 787, 5
Naud M.-E., Artigau É., Doyon R., Malo L., Gagné J., Lafrenière D., Wolf C., Magnier E. A., 2017, AJ, 154, 129
Radigan J., 2014, ApJ, 797, 120
Radigan J., Jayawardhana R., Lafrenière D., Artigau É., Marley M., Saumon D., 2012, ApJ, 750, 105
Radigan J., Lafrenière D., Jayawardhana R., Artigau E., 2014, ApJ, 793, 75
Reid I. N., Cruz K. L., Kirkpatrick J. D., Allen P. R., Mungall F., Liebert J., Lowrance P., Sweet A., 2008, AJ, 136, 1290
Riedel A. R., Blunt S. C., Lambrides E. L., Rice E. L., Cruz K. L., Faherty J. K., 2017, AJ, 153, 1
Rodriguez D. R., Zuckerman B., Kastner J. H., Bessell M. S., Faherty J. K., Murphy S. J., 2013, ApJ, 774, 101
Schneider A. C., Cushing M. C., Kirkpatrick J. D., Mace G. N., Gelino C. R., Faherty J. K., Fajardo-Acosta S., Sheppard S. S., 2014, AJ, 147, 34
Shkolnik E. L., Allers K. N., Kraus A. L., Liu M. C., Flagg L., 2017, AJ, 154, 69
Snellen I., Brandl B., de Kok R., Brogi M., Birkby J., Schwarz H., 2014, Nature, 509, 63
Torres C. A. O., Quast G. R., Melo C. H. F., Sterzik M. F., 2008, in Reipurth B.,ed., Handbook of Star Forming Regions, Vol. II: The Southern Sky, , ASP Monograph Publications, Vol. 5. p. 757
Vigan A. et al., 2012, A&A, 544, A9
Vos J. M., Allers K. N., Biller B. A., 2017, ApJ, 842, 78
Vos J. M., Allers K. N., Biller B. A., Liu M. C., Dupuy T. J., Gallimore J. F., Adenuga I. J., Best W. M. J., 2018, MNRAS, 474, 1041
Wilson P. A., Rajan A., Patience J., 2014, A&A, 566, A111
Zapatero Osorio M. R., Martin E. L., Bouy H., Tata R., Deshpande R., Wainscoat R. J., 2006, ApJ, 647, 1405
Zhou Y., Apai D., Schneider G. H., Marley M. S., Showman A. P., 2016, ApJ, 818, 176
Zhou Y.et al., 2018, AJ, 15, 132
Zuckerman B., Bessell M. S., Song I., Kim S., 2006, ApJ, 649, L115

SUPPORTING INFORMATION

Supplementary data are available at *MNRAS* online.

Appendix.

Please note: Oxford University Press is not responsible for the content or functionality of any supporting materials supplied by the authors. Any queries (other than missing material) should be directed to the corresponding author for the article.

[1] *Department of Astrophysics, American Museum of Natural History, Central Park West at 79th Street, New York, NY 10034, USA*
[2] *SUPA, Institute for Astronomy, University of Edinburgh, Royal Observatory, Edinburgh EH9 3HJ, UK*
[3] *Centre for Exoplanet Science, University of Edinburgh, Edinburgh EH9 3HJ, UK*
[4] *Department of Astronomy, Stockholm University, AlbaNova University Center, SE-106 91 Stockholm, Sweden*

[5] *Institute for Astronomy, University of Hawaii at Manoa, Honolulu, HI 96822, USA*

[6] *Department of Physics & Astronomy and Centre for Planetary Science and Exploration, The University of Western Ontario, London, Ontario N6A 3K7, Canada*

[7] *Utah Valley University, 800 West University Parkway, Orem, UT 84058, USA*

[8] *Department of Physics and Astronomy, Bucknell University, Lewisburg, PA 17837, USA*

[9] *Institute for Astronomy, ETH Zurich, Wolfgang-Pauli-Strasse 27, CH-8093 Zurich, Switzerland*

[10] *Gemini Observatory, Northern Operations Center, 670 N. A'ohoku Place, Hilo, HI 96720, USA*

[11] *IPAG, CNRS/Univ. Grenoble Alpes, F-38000 Grenoble, France*

[12] *Department of Astronomy/Steward Observatory, The University of Arizona, 933 N. Cherry Avenue, Tucson, AZ 85721, USA*

[13] *Max-Planck-Institut fr Astronomie, Knigstuhl 17, D-69117 Heidelberg, Germany*

[14] *Department of Physics, Massachusetts Institute of Technology, 77 Massachusetts Avenue, Cambridge, MA 02139, USA*

[15] *Centre for Astrophysics Research, University of Hertfordshire, College Lane, Hatfield AL10 9AB, UK*

[16] *Zentrum fr Astronomie der Universitt Heidelberg, Landessternwarte, Knigstuhl 12, D-69117 Heidelberg, Germany*

[17] *School of Earth & Space Exploration, Arizona State University, Tempe, AZ 85287, USA*

[18] *NASA Goddard Space Flight Center, 8800 Greenbelt Road, Greenbelt, MD 20771, USA*

This paper has been typeset from a TEX/LATEX file prepared by the author.